POLITECNICO DI MILANO

Master of Science in Biomedical Engineering

Industrial and Information Engineering Department

SPATIOTEMPORAL INVESTIGATION OF THE INFLUENCE OF THE AORTIC ROOT GEOMETRY ON THE HEMODYNAMICS OF A BIOLOGICAL AORTIC VALVE PROSTHESIS USING PARTICLE TRACKING VELOCIMETRY

Supervisor: Prof. Costantino Maria Laura

Co-supervisors: David Hasler, Dominik Obrist

Thesis of:

Leonardo Pietrasanta Matr. 836938

Academic year 2015/2016

Acknowledgments

Thanks to Maria Laura Costantino who has lit up in me the passion for cardiovascular engineering during these two years of master in Politecnico di Milano.

Thanks to Dominik Obrist who gave me the possibility to work in the ARTORG center for Biomedical Engineering Research in the Insel Hospital of Bern.

Thanks to David that supported me during this research period and teached me the meaning of working in fluid dynamics with passion and the smile.

Thanks to all the people working in ARTORG who were always nice and ready to give me a hand.

Thanks to my family that has been always beside me to support my decisions.

Thanks to all my friends with whom I shared wonderful moments here in Switzerland.

Abstract

BACKGROUND: Thousand prosthetic valves are implanted in patients every year relieving them from aortic valve stenosis or insufficiency. One of the most severe complications of valve replacement is prosthetic valve thrombosis.
The hemodynamics through the valve and in the aortic root plays a key role in the pathogenesis of this disease.
OBJECTIVES: The aim of this work is to understand how the geometry of the aortic root affects the fluid dynamics throughout a biological heart valve prosthesis and in the sinus of Valsava.
METHODS: The fluid dynamics investigation focused on a biological Edwards Intuity valve prosthesis and was performed using Particle Tracking Velocimetry.
The Intuity valve was inserted in silicon phantoms suitably casted to reproduce different aortic root geometries and a blood mimicking fluid matching the refracting index of silicone was used. The phantoms with the valves were integrated inside a dedicate test cell in a flow loop simulating the left heart and the systemic circulation.
The test fluid was seeded with microspheres and a high-speed camera was used to acquire images of the seeded fluid during one pulse of the cardiac cycle in the phantoms. The paths of the particles during the cardiac pulse were extracted with ImageJ (Fiji) and successively processed with MATLAB to analyze the flow topology.
RESULTS: Our results show that close to the aortic wall at late systole a backflow forms and enters into the sinus increasing the kinetic energy of the stagnant fluid.
In the sinus, the increment of kinetic energy is associated with a chaotic fluid dynamics and no structured vortex could be observed.
CONCLUSIONS: The geometry of the aortic root influences the strength and the timing of the backflow towards the sinus and the velocity magnitude inside it.
The increment of velocity magnitude caused by the backflow could be a hint for a wash out event of the sinus, but it remains unclear which geometry is preferable to prevent thrombosis.

Sintesi

Migliaia di protesi valvolari sono impiantate ogni anno in pazienti al fine di correggere stenosi o insufficienze della valvola aortica. La trombosi della protesi valvolare è una delle più gravi complicanze derivanti dalla sostituzione valvolare. L'emodinamica attraverso la valvola e nella radice aortica svolge un ruolo chiave nella patogenesi di questa malattia. Lo scopo di questo lavoro è comprendere come la geometria della radice aortica influenza la fluidodinamica di una protesi valvolare biologica e nel seno di Valsalva. L'indagine fluidodinamica è stata effettuata con una protesi valvolare biologica Edwards Intuity utilizzando Particle Tracking Velocimetry.

La valvola Intuity è stata inserita in fantocci in silicone opportunamente fabbricati per riprodurre diverse geometrie di radice aortica ed è stato utilizzato un fluido con le stesse caratteristiche reologiche del sangue e avente l'indice di rifrazione ottica del silicone. I fantocci con le valvole sono stati integrati all'interno di una sezione di prova di un circuito idraulico in grado di simulare il cuore sinistro e la circolazione sistemica. Il fluido di prova è stato seminato con microsfere e una telecamera ad alta velocità è stato utilizzata per acquisire immagini del fluido durante un ciclo cardiaco nei fantocci. Le traiettorie delle particelle durante il ciclo cardiaco sono state estratte con ImageJ (Fiji) e successivamente rielaborate con MATLAB per analizzare la topologia del flusso. I nostri risultati mostrano che, un flusso retrogrado si forma in prossimità della parete aortica a tarda sistole ed entra nel seno aumentando l'energia cinetica del fluido stagnante.

Nel seno, l'incremento di energia cinetica è associato ad una fluidodinamica caotica e non è stato osservato nessun vortice strutturato.

La geometria della radice aortica influenza la velocità e il tempo di comparsa del riflusso verso il seno e il modulo della velocità al suo interno.

In conclusione, l'incremento del modulo della velocità causato dal riflusso potrebbe essere un indizio per il lavaggio del seno, ma rimane non chiaro quale geometria sia preferibile per prevenire la trombosi.

Contents

TITOL ..... **I**

ACKNOWLEDGMENTS ..... **I**

ABSTRACT ..... **III**

SINTESI ..... **V**

CONTENTS ..... **VII**

1.INTRODUCTION **1**

2.BACKGROUND **3**

2.1 ANATOMY AND PHYSIOLOGY OF HEART VALVES 3

2.2 AORTIC VALVE REPLACEMENT 4

2.3 PROSTHETIC HEART VALVE THROMBOSIS 8

2.4 THE ROLE OF THE VALSAVA SINUSES 9

2.5 OBJECTIVE 11

3. MATERIALS AND METHODS **12**

3.1 PARTICLE TRACKING VELOCIMETRY (PTV) 12

3.2 FLOW LOOP 13

3.3 TESTED VALVES 14

3.4 SILICON PHANTOMS 15

3.5 TEST FLUID 18

3.6 SECTION TEST 18

3.7 ACTUATORS & TRANSDUCERS 19

3.7.1 PISTON PUMP 20

3.7.2 PRESSURE MEASUREMENT 21

3.7.3 Flow rate measurement 23
3.8 Trigger 25
3.9 Particles 27
3.10 Illumination 27
3.11 Particles Tracks detection 27
3.12 Valve visualization 34

4.RESULTS 35

4.1 Sinus region 35
4.2 Backflow region 44

5.DISCUSSION AND CONCLUSIONS 51

5.1 The fluid dynamics in the aortic root 51
5.2 The influence of the aortic root geometry 54
5.3 Conclusion and future work 55

BIBLIOGRAPHY 57

Bibliography 57

APPENDIX 61

Appendix 61
A.1 Geometrical parameters relationships 61
A.2 Geometrical parameters in literature 63
A.3 Silicon phantoms fabrication 66
A.4 Refraction Index Matching (RIM) 68
A.5 Particles rest velocity estimation 69
A.6 Camera calibration 70
A.7 Regions Of Interest (ROI) 71
A.8 Jaquaman Linear Assignment Problem 73
A.9 Fiji Linear Assignment Problem 75
A.10 Experimental Protocol 77
A.11 MATLAB scripts 80

1.INTRODUCTION

Thrombosis of a prosthetic valve is one of the most severe complications of cardiac valve replacement. The incidence of prosthetic heart valve thrombosis (PHVT) can be as high as 13% in the first year in any valve position [1] and for prostheses in the aortic position, at any time, the overall incidence is 0.5% [2].

Prosthetic valve dysfunction is a life-threatening condition and prompt treatment is mandatory. Treatment options include anticoagulation, thrombolytic therapy, and surgery.

Heparin anticoagulation therapy is recommended as the initial approach for patients with New York Heart Association (NYHA) functional class I to II status and/or a small thrombus (<0.8 cm2).

Surgery is recommended for patients with NYHA functional class III to IV status and/or a large thrombus (thrombus area > or = to 0.8 cm2). Thrombolytic therapy is recommended if the valve thrombosis persists. Following thrombus resolution and restoration of normal hemodynamics, a regimen of long-term oral anticoagulation could be started to prevent recurrent valve thrombosis [3].

A not physiological hemodynamics throughout the valve prosthesis is one of the major causes of prosthetic valve thrombosis. Turbulent flow can trigger blood damage and platelet activation as stagnant flow can encourage blood clothing [2].

The present in vivo fluid dynamics investigations are patient-specific and only provide limited spatial and temporal resolution.

The aim of this thesis is to investigate the fluid dynamics in the aortic root and in the Sinuses of Valsalva in an in-vitro setup with a bio prosthetic valve and blood

mimicking fluid. Particle Tracking Velocimetry can provide higher spatial and temporal resolutions and more generalized statements due to the user-defined geometry. This two-dimensional technique additionally allows an easy interpretation of the results and facilitates comparison with the medical counterparts.
The study focus on the influence of the aortic root geometry on the flow field. A deeper knowledge thereof could allow in the future to a more correct surgical valve prosthesis implantations and to improve the design of artificial heart valves in order to reduce the incidence of thrombosis.

2.BACKGROUND

2.1 Anatomy and physiology of heart valves

The heart pumps blood through the blood vessels of the circulatory system. Blood provides the body with oxygen and nutrients, as well as assists in the removal of metabolic wastes. The heart has four chambers, two upper atria, the receiving chambers, and two lower ventricles, the discharging chambers.

Commonly the right atrium and ventricle are referred together as the right heart and their left counterparts as the left heart (Fig. 2.1.1). As the heart is not a continuous pump, valves are necessary to sustain a unidirectional blood flow allowing blood to flow in and out of the respective chambers. One valve lies between each atrium and ventricle, and one valve rests at the exit of each ventricle.

The valves between the atria and ventricles are called the atrioventricular valves.

The tricuspid valve separates the right atrium and the right ventricle and has three cusps connected to three papillary muscles.

The mitral valve lies between the left atrium and left ventricle. It is also known as the bicuspid because it has two leaflet, an anterior and a posterior cusp. These cusps are also attached via chordae tendinae to two papillary muscles.

Two additional semilunar valves with three cusps sit at the exit of each of the ventricles: the pulmonary valve located at the base of the pulmonary artery and the aortic valve settled at the base of the ascending aorta.

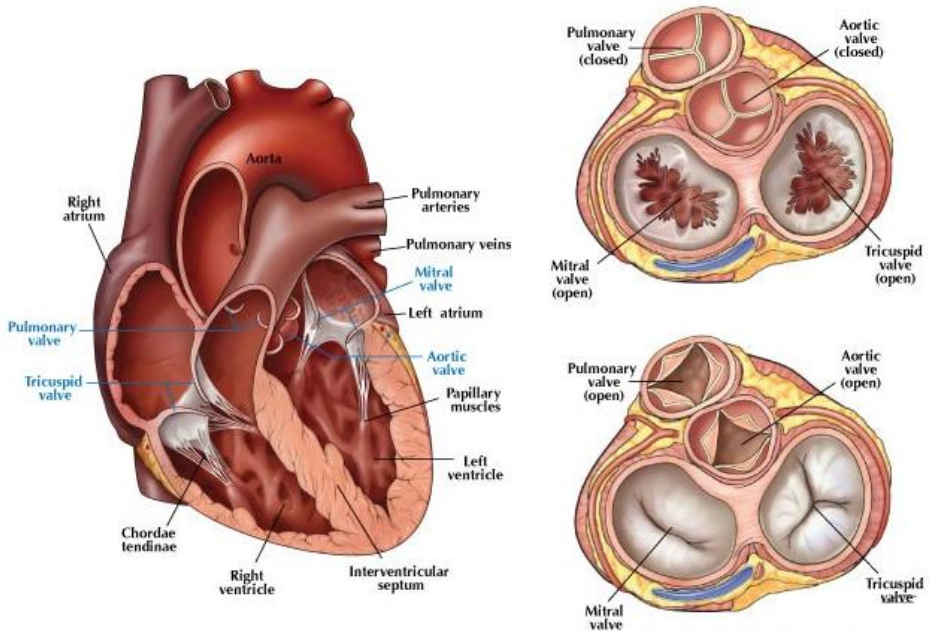

Figure 2.1.1: Sections of a heart showing the heart valves (courtesy of [4]).

2.2 Aortic valve replacement

The aortic valve (Fig. 2.2.1) is designed to ensure unidirectional blood flow from the left ventricle into the aorta during systole and to prevent retrograde blood flow from the aorta to the left ventricle during diastole.

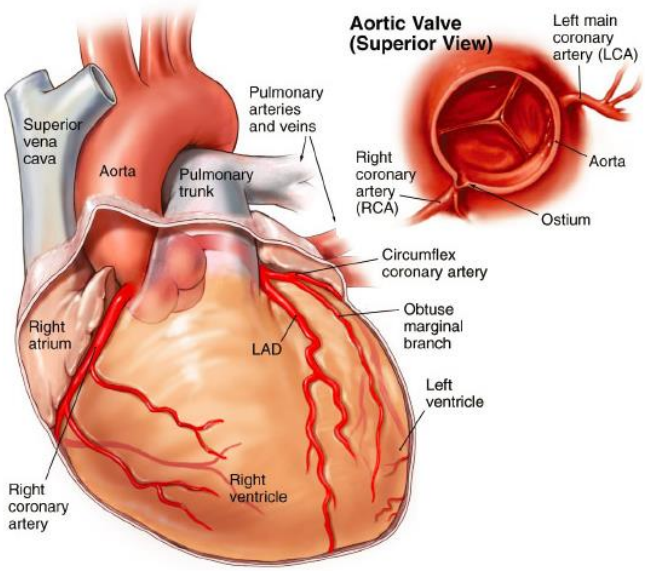

Figure 2.2.1: Aortic root and coronaries (courtesy of [5]).

As depicted in the Fig. 2.2.2 during the heart cycle the aortic valve opens when the ventricular pressure overcome the aortic pressure at the beginning of the systole or end of diastole and start closing when the flow between the leaflets decelerates, such that it reaches the closed position when the flow direction reverses at the end of systole or beginning of the diastole.

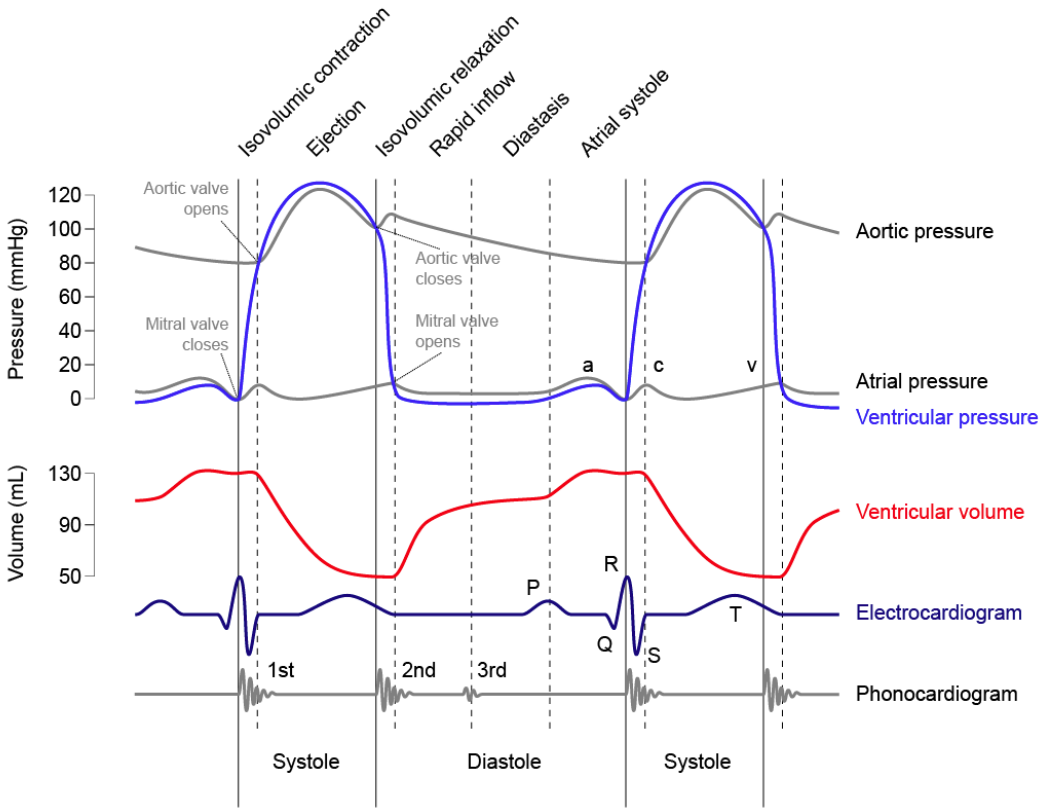

Figure 2.2.2: Heart cycle (courtesy of [6]).

The structural and functional abnormalities of the aortic valve can give rise to various valve diseases that can affect the normal operation of the entire heart. The main diseases of the aortic valve are stenosis and insufficiency.

Aortic insufficiency is the inability of the valve to close completely during the diastolic phase of the cardiac cycle, generating a reflux of blood from the aorta to the left ventricle.

Globally, due to aortic valve insufficiency, the stroke volume that has to be pumped by the heart increases because a fraction of the blood ejected during systole in the aorta comes back in the left ventricle. The malfunctioning of the valve triggers an

adaptive response that changes the structure and geometry of the heart muscle. To maintain an adequate ejection fraction to perfuse all peripherals districts of the body the left ventricle undergoes eccentric hypertrophy.
Aortic stenosis is a narrowing of the valve orifice which obstructs the physiological blood flow from the left ventricle into the aorta during systole.
Globally, the pressure that must be generated by the ventricle in order to overcome the resistance offered by the stenotic aortic valve is increased.
Also in this case, the malfunctioning of the valve triggers an adaptive response that changes the structure and geometry of the heart muscle. To maintain an adequate ejection fraction to perfuse all peripherals districts of the body the left ventricle undergoes concentric hypertrophy.
With the worsening over years of eccentric hypertrophy in case of aortic valve insufficiency and concentric hypertrophy in case of aortic valve stenosis the heart may undergoes ischemia and failure.
Stenosis and insufficiency can have different etiology: they may result from congenital malformations present from birth or they may be acquired during the lifetime of the subject. Among the main acquired causes there are wear, calcification, inflammation, and infection of the valve, or much more rarely trauma.
If the disease of the aortic valve is severe conventional therapy involves surgery to replace the natural valve.
For the replacement of natural valves two main types of artificial valves are used: rigid-leaflet or mechanical valves (Fig. 2.2.3.a), made of synthetic materials, and flexible leaflet (Fig 2.2.3.b) or biological valves, made either with porcine or bovine pericardium.

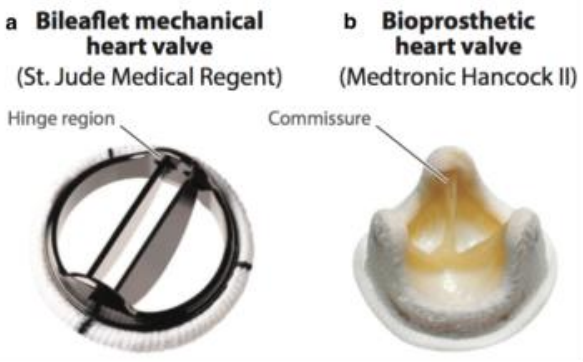

Figure 2.2.3: Mechanical (a) and biological (b) aortic heart valves (courtesy of [7]).

In general, the prosthetic valves used in replacements, whether biological or mechanical, must meet some basic design requirements. First, they must ensure the correct unidirectional motion of the blood from the left ventricle to the aorta under the action of the physiological pressure gradients for at least 10 years. They must also be biocompatible, haemocompatible, radiopaque, quiet and available in various sizes. Not less important are the requirements concerning the pressure drop and the regurgitation flow rate that, for the aortic valve, must not exceed respectively 15-20 mmHg and 20% of the ejected volume.

Mechanical valves are an important part of the market of implantable aortic valve prostheses and despite not having the shape of natural valves they are able to replace their functionality for a long time, about 30 years. This characteristic, in many clinical cases makes mechanical valves preferable to other valve prostheses available. However, these valves also have some disadvantages: they force patients to undergo anticoagulation therapy, they are noisy, hemolytic, the fluid dynamics of blood is disturbed and a sudden rupture is fatal for the patient.

On the contrary biological valves, in spite of a shorter life, allow to have more physiological fluid dynamics, are quiet and the anticoagulant therapy is not mandatory.

Furthermore, while mechanical valves can only be implanted surgically, biological valves prosthesis are also available for percutaneous implantation via a catheter (Trans catheter Aortic Valve Implantation, TAVI).

A negative aspect of the biological heart valve prostheses is that they are affected to the same degeneration processes of natural valves but even though they are not radiopaque they can be investigated trough regular diagnostic techniques [8].

Whether necessary, the type of valve to be implanted is determined by clinicians based on the patient's clinical picture.

During the gold standard surgical procedure of valve replacement, the surgeon removes the patient's diseased aortic valve and put a mechanical or biological valve in its place.

2.3 Prosthetic heart valve thrombosis

A great variety of designs of prosthetic heart valves have been used since 1950. Refinements in valve design and progress in operating technique have dramatically improved the prognosis of patients subjected to heart valve replacement surgery. Thromboembolic complications, however, remain a troublesome cause of post-operative morbidity and mortality [3].

The incidence of prosthetic heart valve thrombosis (PHVT) can be as high as 13% in the first year in any valve position. At any time, for prostheses in the aortic position, the overall incidence is 0.5% to 6% per patient-year [2].

The New York Heart Association (NYHA) has classified PHVT in functional classes from I to IV. I or II are not obstructive forms, usually incidental echocardiographic findings in patients with evidence of thromboembolic stroke or peripheral arterial embolism. Those classified as classes III or IV correspond to obstructive forms with obvious haemodynamic repercussions, sometimes including cardiogenic shock, often associated with cerebral or peripheral embolism.

Transesophageal echocardiography (TEE) is an efficient diagnostic tool to determine alterations in the occlusive mechanism or the existence of valvular thrombotic masses. TEE may also be useful to differentiate thrombus from pannus as mechanism of prosthetic obstruction [1]. In prosthetic thrombosis, the movement of the disc is always abnormal, whereas in 40% of patients with obstruction due to pannus the mobility of the disc is normal. The visualization of an echogenic mass is almost universal in thrombosis, but only appears in 70% of obstructions caused by pannus. The echogenic characteristics of the mass are more important: it has an appearance of soft tissue (thrombotic material) in thrombosis, while it appears as hard tissue (fibrotic material) in the case of pannus. A thrombotic mass is usually larger than pannus.

The pathogenesis of intracardiac thrombus formation is complex: can be triggered by the direct contact of the surface of the prosthesis with the blood stream, can derive from an inadequate anticoagulation treatment or can be the consequence of an altered transprosthetic blood flow [9].

All currently implanted mechanical cardiac devices generate flow patterns that are significantly different from those present in a normal cardiovascular system. Typically, these flow patterns include regions of high velocity and high shear that are

potentially damaging to blood elements, as well as recirculation regions with long flow residence times where clot formation may occur.
Although biological heart valve prosthesis have a more natural fluid dynamics it is important to point out that they are also subject to thrombosis phenomena [3].

2.4 The role of the Valsava sinuses

The aortic sinuses are anatomical dilations present in the very first part of the ascending aorta, which occur just above the aortic valve. These widenings, that are also commonly called sinuses of Valsava, form three hemispherical pockets between the wall of the aortic root and each of the three cusps of the aortic valve.
In physiological condition, there are three aortic sinuses: the left aortic sinus that gives rise to the left coronary artery, the right aortic sinus that gives rise to the right coronary artery and the posterior sinuses from where no vessels arise.
Many studies have shown that the presence of sinuses of Valsava influences the kinematics of the valve leaflets: in particular, the importance of the sinuses of Valsava has been considered to achieve smooth opening and closing movements of the aortic valve leaflets [10], [11], [12].
However contradictory interpretations are provided in the literature about the fluid dynamics event taking place in the sinuses.
Leonardo da Vinci was the first to investigate in detail the fluid dynamics in the sinuses and to hypothesize the presence of an Aortic Sinus Vortex (ASV) [13].
A first interpretation of the ASV was proposed by B.J.Bellhouse and colleagues who suggested that the sinuses have the function to host and expand the ASV.
According to B.J.Bellhouse and colleagues the ASV follows the ejected flow in proximity of the root axis and has opposite direction close to the arterial wall as depicted in the following Fig.2.4.1 [14], [15].

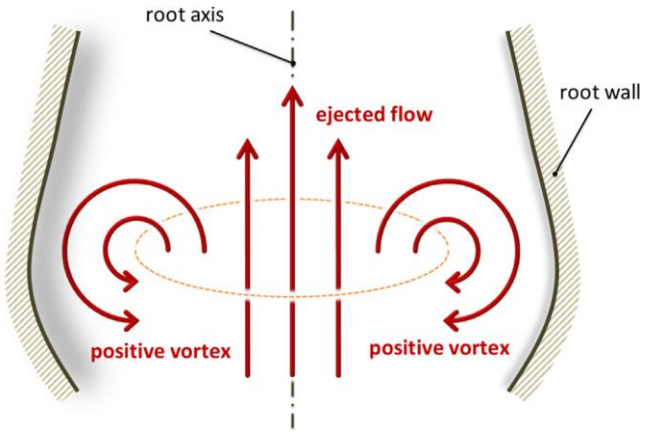

Figure 2.4.1: Aortic Sinus Vortex according to B.J.Bellhouse and colleagues (courtesy of [16]).

The presence of these trapped vortices in the aortic sinuses would play two distinct roles in the valve operation.

During the period of maximum velocity in the aorta, when the valve is fully opened and the flow is quasi-steady, it would act as a control system maintaining the valve cusps in a static fully opened configuration with the cusp tips protruding slightly into the sinus cavities.

In the closure phase of the cycle, the trapped vortices would persist because of their long decay time and would contribute to the prevention of jet formation from the narrowing valve opening.

Evidence of the ASV has been reported in more recent in vitro [17] and in vivo [18] studies.

Despite the general consensus of the presence of the ASV in the valve opening stage its evolution during the heart pulse is controversy.

Other researchers indeed, find out the ASV generated during the valve opening is convected away towards the aorta and a secondary vortex with opposite rotation forms and remains within the sinus until the valve begins to close [19].

Furthermore, the latest studies show a more complex scenario characterized by a high 3-dimensional fluid dynamics [20], [7].

It has been further demonstrated that the presence of these vortices, their duration and topology, can be affected in space and time by the presence of the coronaries flow [17] and by the shape of the aortic root [16].

Toninato shows how the intensity, location and duration of the vortices present in the sinuses vary in dependence of the condition of implantation of the valve and the geometry of the sinuses themselves.
Querzoli shows that the coronary flow washes away the vortices present in the sinuses reducing their impact on the leaflets of the valve.
The difference in the literature findings can be explained in light of the lack of a standard for the in vitro experiments. Moreover, the spatial and temporal resolution of present-day 4D-MRI techniques do not allow to capture in vivo the dynamics of the vortices in the sinuses [19].
Therefore, although it is now accepted that the fluid dynamics in the sinuses is influenced by the geometry of the aortic root and the presence of the coronaries, further studies are necessary to understand which geometrical parameters have impact on it. A deeper knowledge is indeed necessary to optimize valve implantation conditions and washout to reduce thrombosis and valve failure.

2.5 Objective

Object of this work is to investigate the fluid dynamics in the aortic root and to understand how the shape and geometry of the aortic root affects the fluid dynamics in the Sinuses of Valsava.
Specifically, a spatiotemporal investigation of the influence of the geometry of the sinuses of Valsava on the hemodynamics of a biological Intuity aortic valve prosthesis is performed using Particle Tracking Velocimetry (PTV).

3. MATERIALS AND METHODS

3.1 Particle Tracking Velocimetry (PTV)

The hemodynamics in the sinuses depends on the geometry of the aortic root and on the presence of the coronaries flow as mentioned in the previous section but it is also strongly influenced by the compliance of the aortic root, the design and orientation of the valve, the viscosity of the test fluid, the heart rate and stroke volume.

Since the aim of the study was to investigate the influence of the geometry of the aortic root on the fluid dynamics of a biological heart valve prosthesis only one size of valve was used and the compliance of the aortic root and the presence of the coronary flow were not taken into account as experimental variables.

For the experimental campaign, an Edwards Intuity valve (Edwards Lifesciences, Irvine, USA) was used and preliminary tests with a Furtiva trileaflets mechanical valve were conducted.

The valves were inserted in silicon phantoms suitably casted to reproduce different postoperative implantation sceneries and a blood mimicking fluid of water, glycerol and sodium chloride matching the refracting index of silicone was used.

The phantoms with the valves positioned inside them were integrated inside a dedicate test cell in a flow loop simulating the left heart and the systemic circulation. Pressure transducers and ultrasonic flow meters were installed to monitor hydraulic quantities during measurements.

The test fluid matching the viscosity of blood was seeded with microspheres with a diameter of 200 μm.

A PHOTRON-ultima video camera was used to acquire images at 2000 fps of the seeded RIM fluid during one pulse of the cardiac cycle.
The acquired images were preprocessed in MATLAB to perform a background removal and further processed with ImageJ (Fiji) to track the path of the particles during the cardiac pulse. The particles tracks extracted with ImageJ (Fiji) were successively post processed with MATLAB to extract information of the velocity field and topology [21]. It has to be noted that what could be seen in the images was the projection of the particles on the image plane so that it was not possible to compute the out of plane velocity component and only the horizontal and vertical component of the particles velocity where considered for the flow field analysis.

3.2 Flow Loop

The bench test was a flow loop (Fig. 3.2.1) reproducing the left side of the heart and the systemic circulation.
The synthetic ventricle was rigid and reproduced the physiological contraction thanks to the action of a volumetric piston pump to which it was connected.
During systole, the fluid was driven, towards the compliance chamber throughout the valve that was settled into the silicon phantom.
The arterial compliance of the whole systemic circulation was reproduced with a rigid plexiglass box partially filled with air, while for the total peripheral resistance a tap was used.
Changing the volume of air present in the compliance and regulating the opening of the tap it was possible to trigger the value of the total compliance and of the total resistance of the mock loop.
From the compliance, the fluid was reaching a synthetic atrium chamber at atmospheric pressure passing throughout the resistance of the tap.
During diastole, the fluid in the synthetic ventricle was filling the synthetic ventricle passing throughout a bileaflets mechanical valve that reproduced the functionality of the mitral valve.

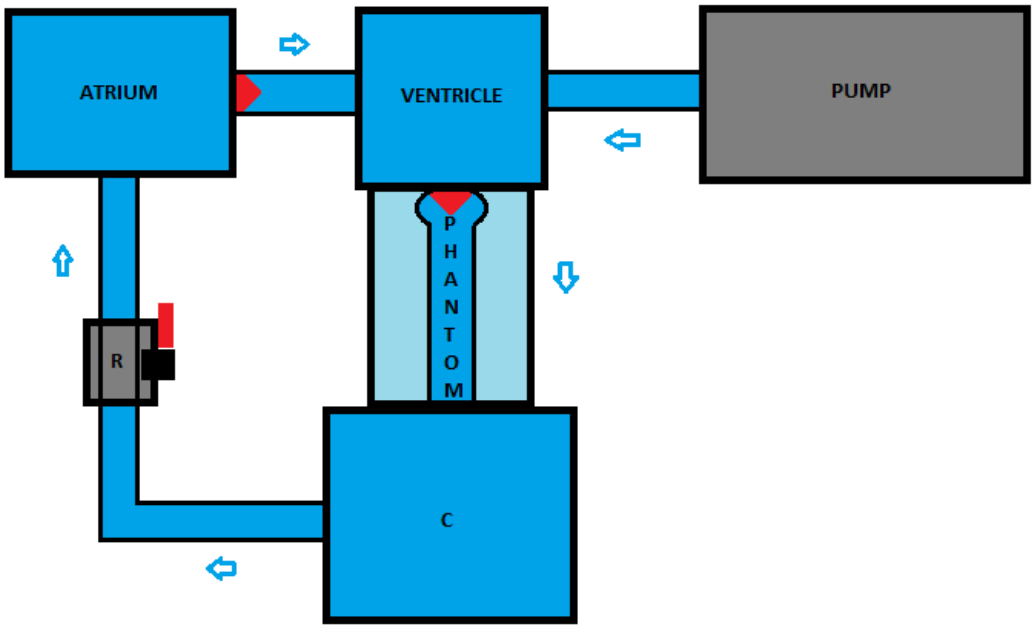

Figure 3.2.1: Scheme of the flow loop.

3.3 Tested valves

The experiments were conducted with an Edwards Intuity valve (Edwards Lifesciences, Irvine, USA) with a nominal diameter of 21 mm with bovine pericardium leaflets, an alloy cage for the commissures and a stainless-steel frame allowing implantation with a balloon catheter.

In clinical practice the valve is additionally fixed with three sutures to secure its position and orientation in the aortic root.

In the experimental setup, the valve was implanted in an aluminum socket with a diameter of 22 mm and an inlying O-ring with an inner diameter of 21 mm representing the aortic annulus. Preliminary experiments were conducted with a Furtiva three leaflets mechanical valve.

Figure 3.3.1: Intuity valve to the right and Furtiva valve to the left.

3.4 Silicon phantoms

To mimic the aortic root, silicon phantoms were casted according to a standard geometry that had to be defined. The lack of a unified aortic root representation indeed can lead to wide range of predicted fluid dynamics behaviors and affect further research efforts.

R.Haj-Ali et al. [22] reviewed the existing literature on the topic and proposed a parametrized geometry, which was also verified with three-dimensional trans-esophageal echocardiography (3D-TEE) at mid diastole.

Among various articles, R.Haj-Ali et al. review the paper of Swanson and Clark [23] that had been used as referment in many works and the paper of Reul et al. [24] in which a two-dimensional (2D) description of the aortic root was constructed from sections of angiography measurements.

In the present study, starting from the findings of the cited works, a simplified representation of the aortic root was defined.

In the Fig. 3.4.1 is reported the chosen aortic root geometry with the geometric parameters of interest. In the picture the annulus radius r_r, the commissure radius r_{co}, the sinus radius r_s, the sinotubular junction radius r_{STJ} and the two height of the sinus h_1 and h_2 are reported.

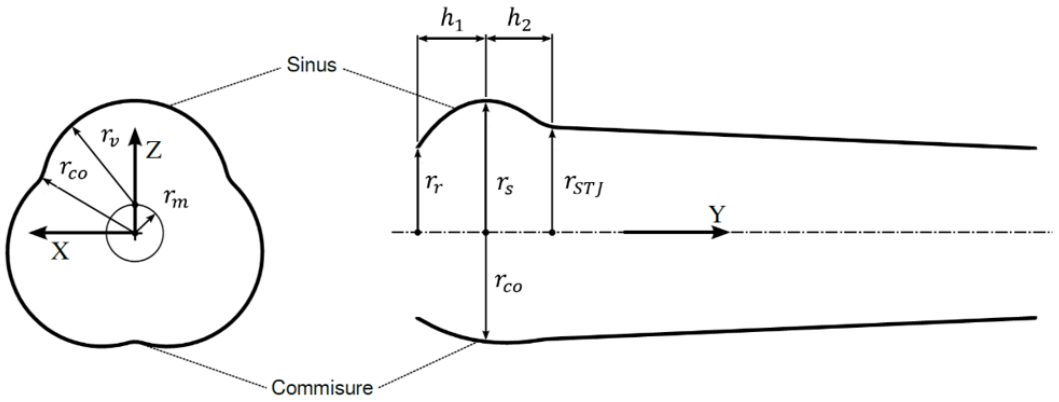

Figure 3.4.1: Aortic root geometry considered for the experiment campaign.

The geometry of the aortic root was parametrized based on the root annulus r_r. To do so the following scaling parameters were defined:

$$\alpha_s = \frac{D_s}{D_r} = \frac{r_s}{r_r}$$

$$\alpha_{co} = \frac{D_{co}}{D_r} = \frac{r_{co}}{r_r}$$

$$\alpha_A = \frac{D_{STJ}}{D_r} = \frac{r_{STJ}}{r_r}$$

$$\alpha_L = \frac{h_1 + h_2}{D_r} = \frac{h_1 + h_2}{2r_r}$$

$$\alpha_{h_1} = \frac{h_1}{D_r} = \frac{h_1}{2r_r}$$

As can be seen from the previous image (Fig. 3.4.1) to define the geometry it was necessary to define the constructive radii r_m and r_v.
To make also these two last parameters dependent only on the scaling parameters the following geometrical relationships were considered:

$$r_m = \frac{r_r(\alpha_{co}^2 - \alpha_s^2)}{\alpha_{co} - 2\alpha_s}$$

$$r_v = \frac{r_r(\alpha_{co}\alpha_s - \alpha_{co}^2 - \alpha_s^2)}{\alpha_{co} - 2\alpha_s}$$

A more detailed description about geometrical parameters relationships can be found in Appendix A.1.

To obtain three different phantoms seizes to be tested with the valve different values of the above reported scaling parameters were considered.

In the Table 3.4.1 the chosen scaling parameters of this work are reported:

INPUT	Small geometry	Medium geometry	Large geometry
αs	1,395	1,55	1,705
αA	1,125	1,25	1,375
αL	0,675	0,75	0,825
αh1	0,315	0,35	0,385
αco	1,125	1,25	1,375

Table 3.4.1: Chosen scaling parameters.

Although it's difficult to make a comparison with the literature because of the different aortic root geometries that are used and of the different way how the geometrical parameters are measured, Appendix A.2 give an idea of the difference between the chosen scaling parameters and the ones reported in the cited literature.

The aortic root and a short section of the ascending aorta were modelled with silicone phantoms according to the above described geometry. Negatives of the three different sizes of the chosen geometry were manufactured using 3D printing process. Successively the negatives were sandpapered, treated with spot filler and varnished to increase the surface properties.

Starting from the three-different 3D printed negatives, thick-walled silicone phantoms were casted using ELASTOSIL RT 601 (Wacker Silicones, Germany) which has very good transparency properties and a refraction index of n=1:41.

A more detailed guide about silicon phantoms casting can be found in Appendix A.3.

Figure 3.4.2: 3D printed negatives to the left and silicon phantoms to the right of the three different geometries.

3.5 Test Fluid

A blood mimicking fluid composed of water, glycerol and sodium chloride was used. The obtained fluid resulted to have viscosity and rheological properties close to blood while retaining the ability to match the refractive index of the silicone phantoms. In such a way, it was possible to have a direct visual access inside the silicon phantoms with a negligible distortion due to the refraction index inhomogeneities.
The refractive index matching (RIM) procedure has been used in previous work [25], [26] and it is reported in more detail in the Appendix A.4.
The kinematic viscosity ν_f and the density ρ_f of the tested fluid resulted to be $4.2 * 10^{-6}\ m^2/sec$ and $1{,}2 * 10^3\ kg/m^3$ respectively. This means that the dynamic viscosity $\mu_f = \nu_f * \rho_f$ was equal to $5{*}10^{-3}\ Pa * sec$.

3.6 Section Test

The silicone phantoms were placed in a transparent housing made of PMMA with high transparency properties allowing optical access into the sinus. The void between the test cell and the phantom was filled with index matched fluid.
The inlet and the outlet of the phantom were placed over aluminum tappets to connect them to the rest of the mock loop.
The tested valve was settled in the aluminum tappet at the inlet of the silicon phantom. Additionally, two clamping rings were placed around the phantom to prevent leakages.

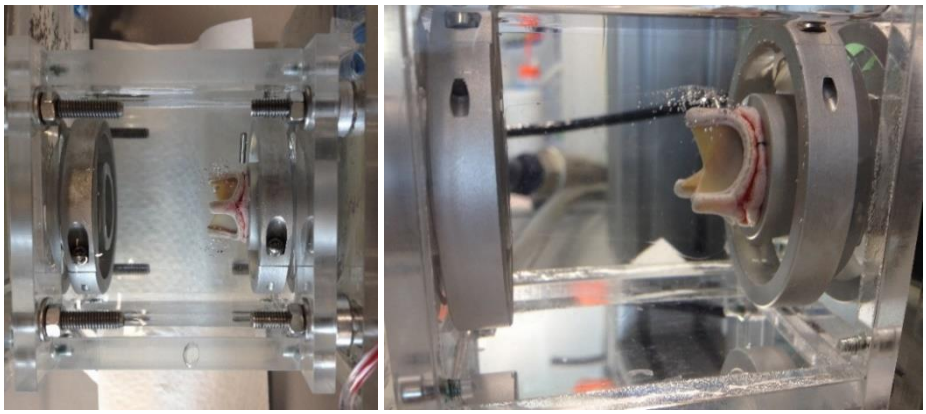

Figure 3.6.1: Upper view to the left and side view to the right of the section test filled with RIM fluid.

3.7 Actuators & Transducers

As mentioned, pressure transducers and ultrasonic flow meters were installed to monitor hydraulic quantities and a front and a side high speed cameras were used to acquire images of the valve and of the sinuses respectively (Fig. 3.7.2).

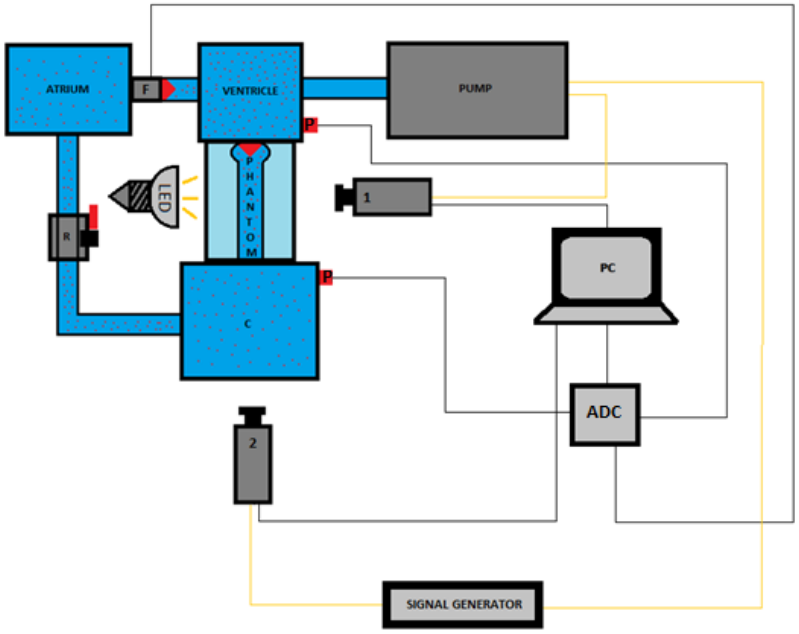

Figure 3.7.1: Scheme of the experimental set up.

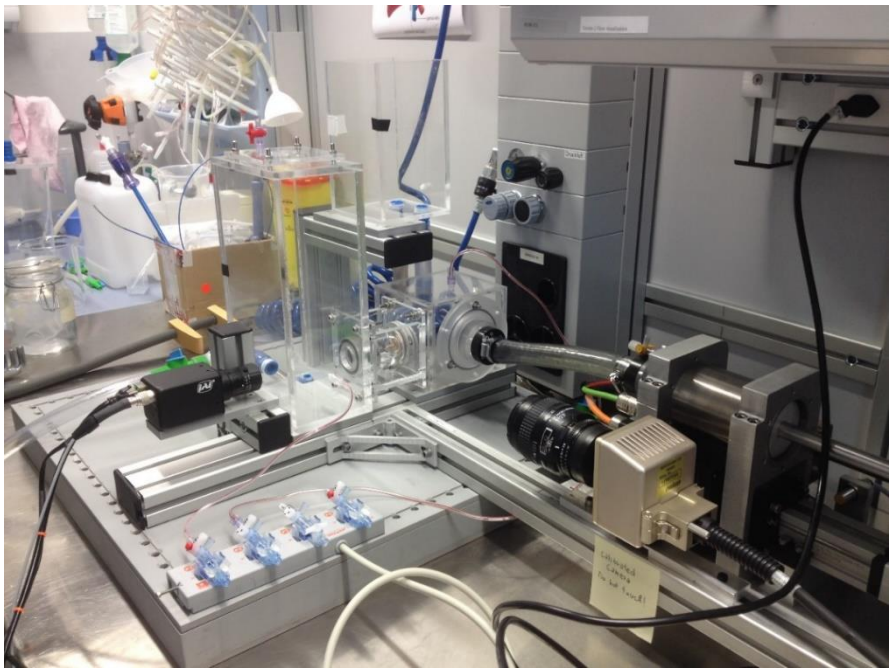

Figure 3.7.2: Photo of the experimental set up.

3.7.1 Piston Pump

The experiments were conducted under a pulsatile flow conditions, based on the physiological flow profile provided by the piston pump (Fig 3.7.1.1).
Through the software Motion Basic, the heart rate and the amplitude of the flow were prescribed. All the experiments were conducted with a heart rate of 72 bpm and a mean velocity of 1 m/s at peak flow.

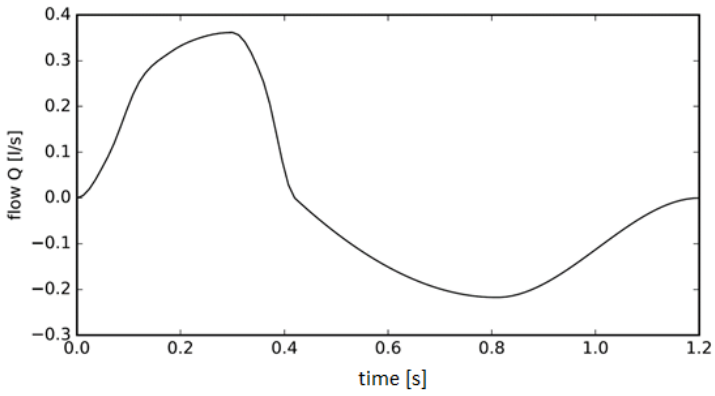

Figure 3.7.1.1: Profile of the flow rate signal furnished by the piston pump.

3.7.2 Pressure measurement

The pressure was measured upstream the tested valve in the synthetic ventricle (transducer V in figure 3.6) and downstream the silicone phantom in the compliance chamber (transducer A in figure 3.6) thus providing the ventricular and the aortic pressure, respectively. The transducers were connected to an Analog to Digital Converter (ADC). An example of pressure signals acquired during the measurement is reported in Fig. 3.7.2.1.

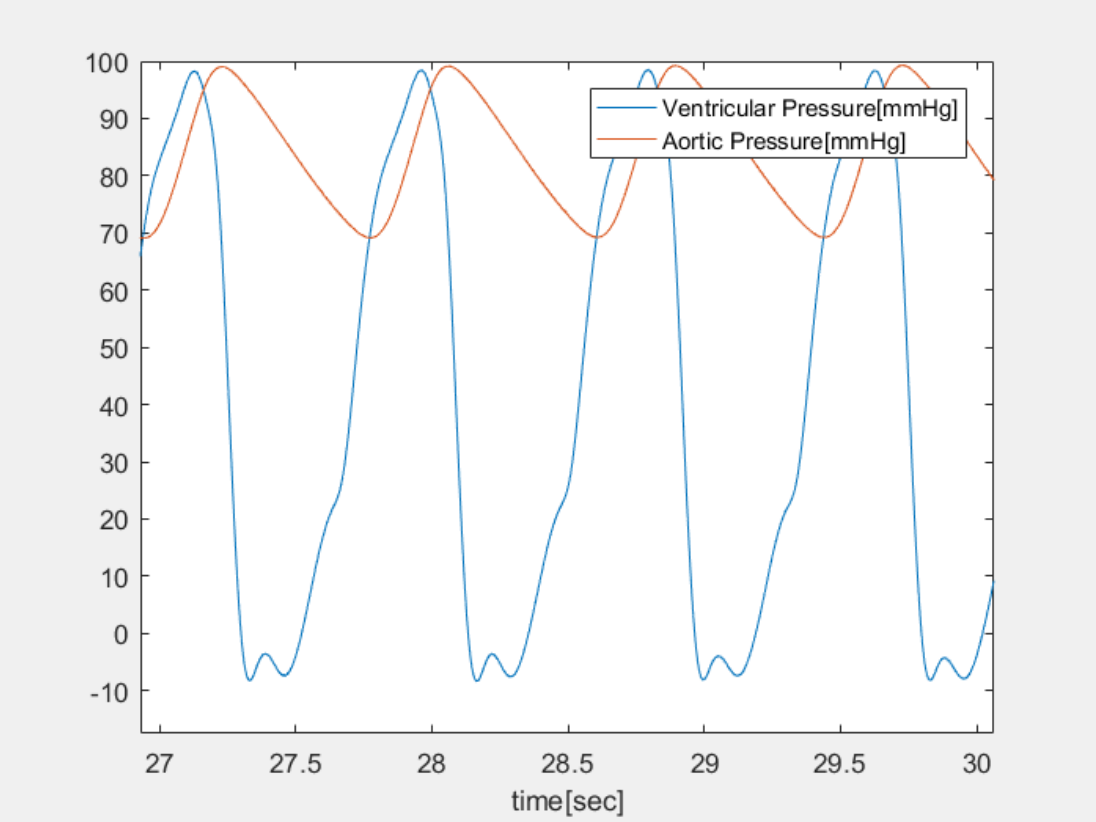

Figure 3.7.2.1: Ventricular and Aortic pressure signals.

The mock loop as employed was able to reproduce physiological pressure signal with an aortic pressure range between -10 and 100 mmHg and a ventricular pressure range between 70 and 100 mmHg. Even though the absolute value of the ventricular

pressure signal and of the aortic pressure signal are not in the physiological ranges the fluid dynamics in the section test undergoes physiological pressure conditions because the difference between the ventricular pressure signal and aortic pressure signal is in the physiological ranges.

The acquired pressure signals once amplified and filtered in the Amplification Box were directed in to an Analog to Digital Converter and visualized using LabVIEW.

In Fig 3.7.2.2 and Fig. 3.7.2.3 the pressure signals applied during the experiments for the three different geometries are overlapped to visualize the reproducibility of the pressure experimental conditions.

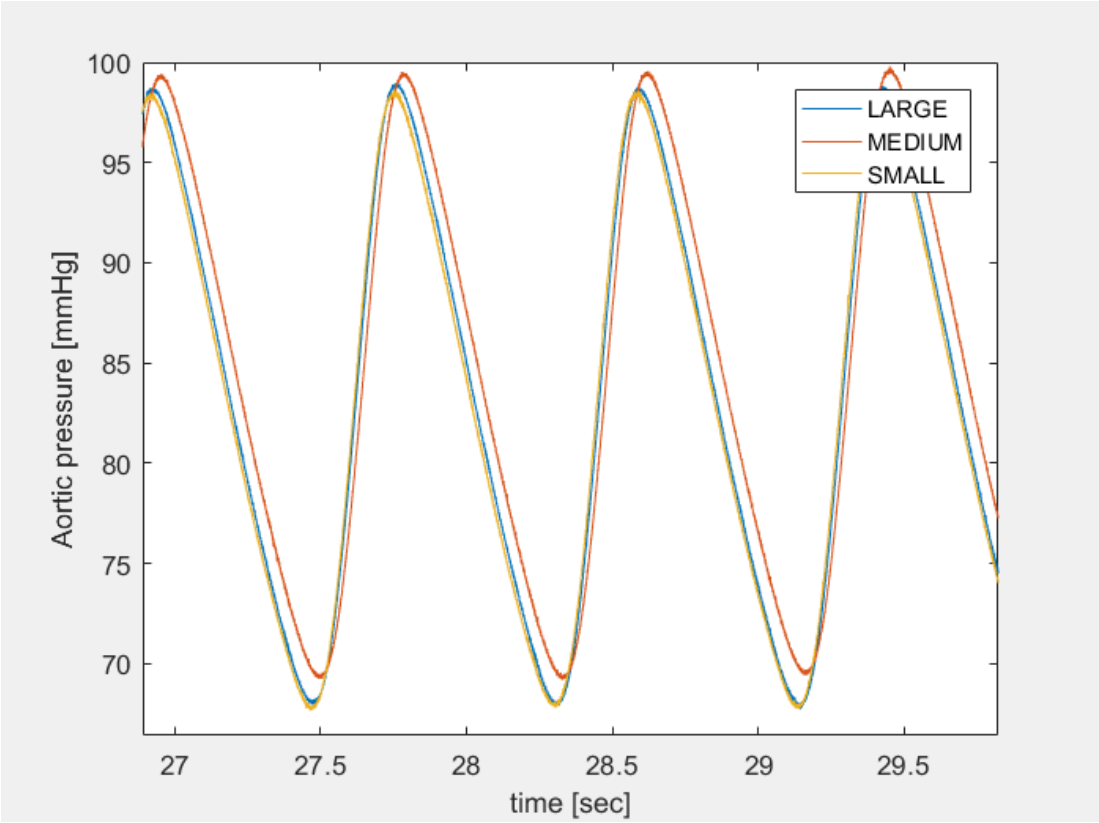

Figure 3.7.2.2: Aortic pressure signals of the three different geometries.

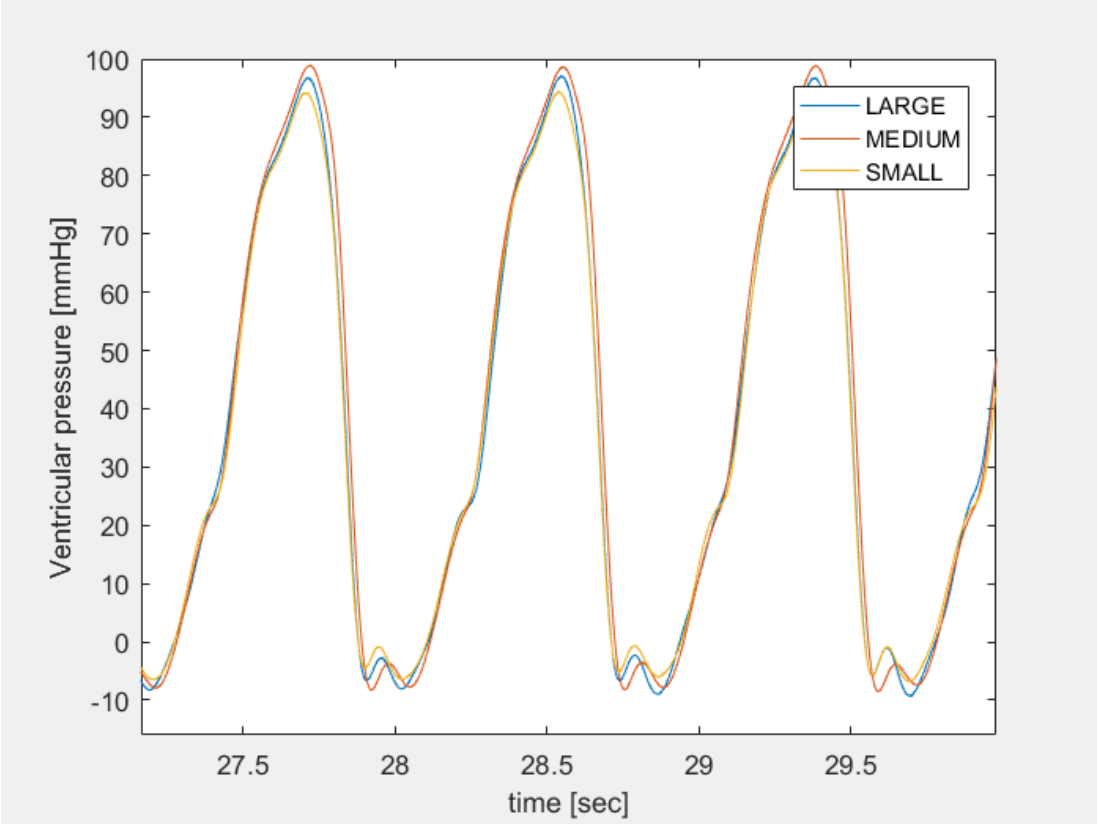

Figure 3.7.2.3: Ventricular pressure signals of the three different geometries.

3.7.3 Flow rate measurement

The only place where the ultrasonic flow sensor TS410 Flowmeter (Transonic Systems Inc, Ithaca NY, USA) could be placed was before the bileaflet mechanical heart valve prosthesis on the tube linking the atrium chamber with the synthetic ventricle. As for the pressure signals, the acquired flow signals were directed in to a ADC and visualized using LabVIEW.

The actual aortic flow rate was computed summing to the flow rate measured by the TS410 Flowmeter the flow rate given by the piston pump:

$$Q_{aorta} = Q_{flow\ meter} + Q_{piston\ pump}$$

where $Q_{flow\ meter}$ represent the flow through the bileaflet, Q_{aorta} the flow through the Intity valve and $Q_{piston\ pump}$ the flow given by the piston pump.

The flow rate given by the piston pump was calculated recording the displacement of the piston and knowing the geometrical dimension of the pump and the heart rate:

$$Q = v * A = \frac{\Delta x}{\Delta t} * A = \frac{\Delta x * 2 * \pi * r_p^2}{\frac{60}{f}} \; [m^3/sec]$$

where Δx [m] is a discrete increment of the pump piston, r_p [m] is the radius of the cylinder of the piston pump, and f [bpm] is the heart rate.
An example of the computed aortic flow rate signal is reported below in Fig 3.7.3.1.

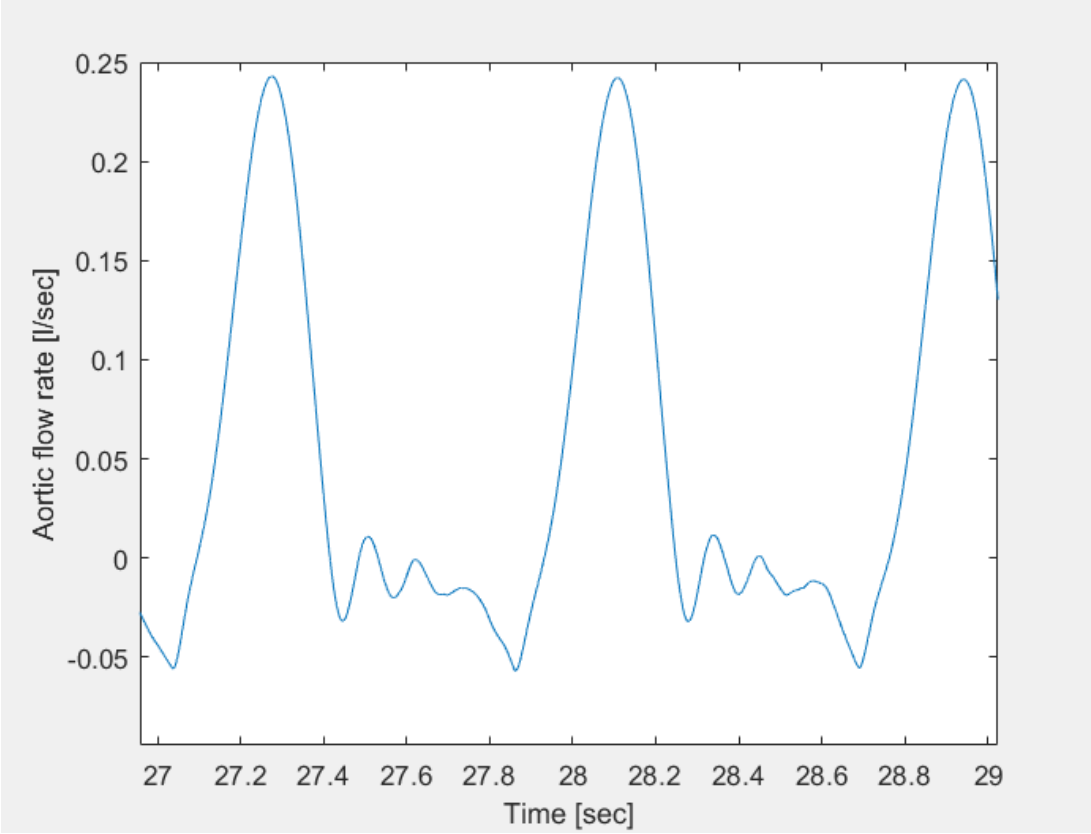

Figure 3.7.3.1: Aortic flow rate signal.

It has to be noted that the used TS410 Flowmeter is not designed for pulsatile flow but for steady and developed flow, so that oscillations were introduced in the flow rate measurement.

In Fig. 3.7.3.2 the flow rate signals acquired by the TS410 Flowmeter in the experiments related to the three different geometries are overlapped to visualize the reproducibility of the flow experimental conditions.

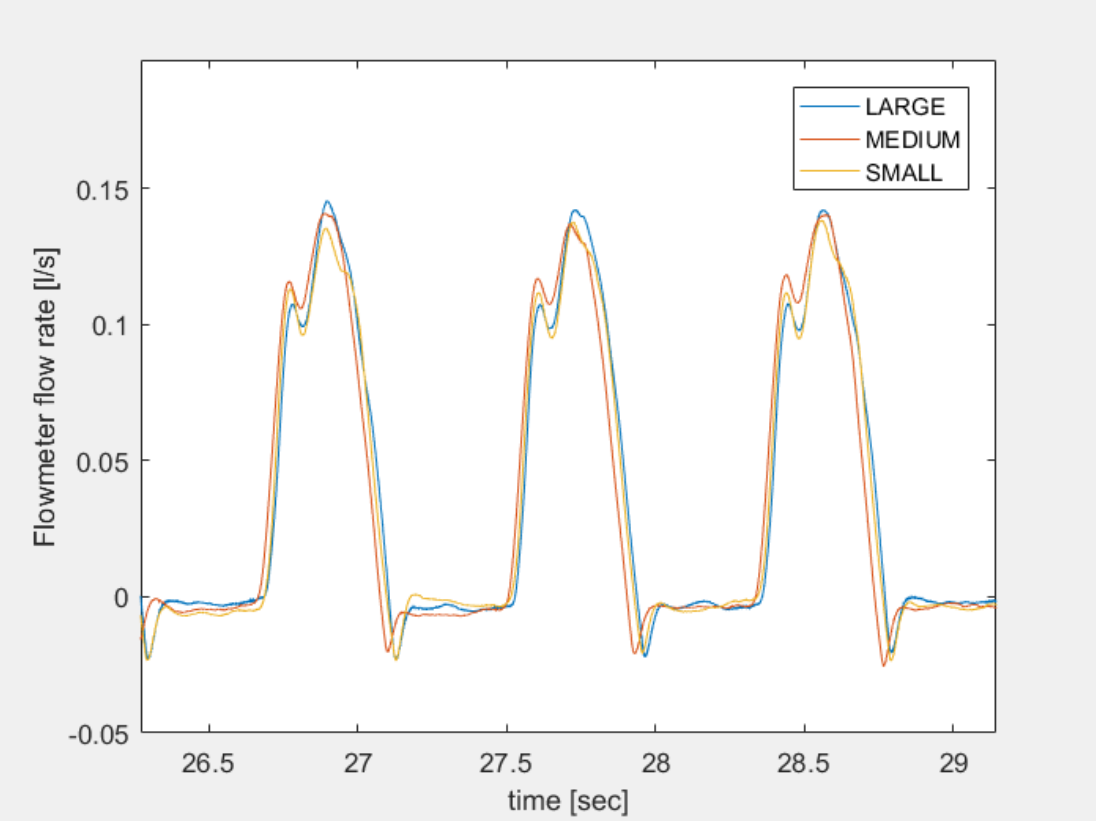

Figure 3.7.3.2: Flow rate signal of the three different geometries registered by the TS410 Flowmeter.

3.8 Trigger

To synchronize the acquisition of data and start the recording of images at the same instant a trigger signal was needed. So, an electronic triggering circuit was built: a trigger signal was taken from the piston pump in correspondence of the 30^{th} pulse and sent to the cameras.

In Fig. 3.7.1 the side high-speed camera N°1 was a PHOTRON-ultima video camera while the front camera N°2 was a Jai TM-6740 GE CCD camera. To make the Jai TM-6740 GE CCD camera working it was necessary to trigger for each image acquisition.

For that, it was necessary to introduce a signal generator that once received the trigger signal from the piston pump would send a burst of 1000 cycles at a frequency of 200 Hz to the Jai TM-6740 GE CCD camera. This intermediate triggering step wasn't necessary for the PHOTRON-ultima camera that could be directly triggered exploiting the trigger signal from the piston pump.
The trigger signal was visualized and recorded in LabVIEW as a reference for the recorded flow rate and pressure measurements.
The electronic triggering circuit is schematized in the Fig. 3.7.1 with the yellow lines while an example of the trigger signal coming out from the pump is reported in Fig 3.8.1.

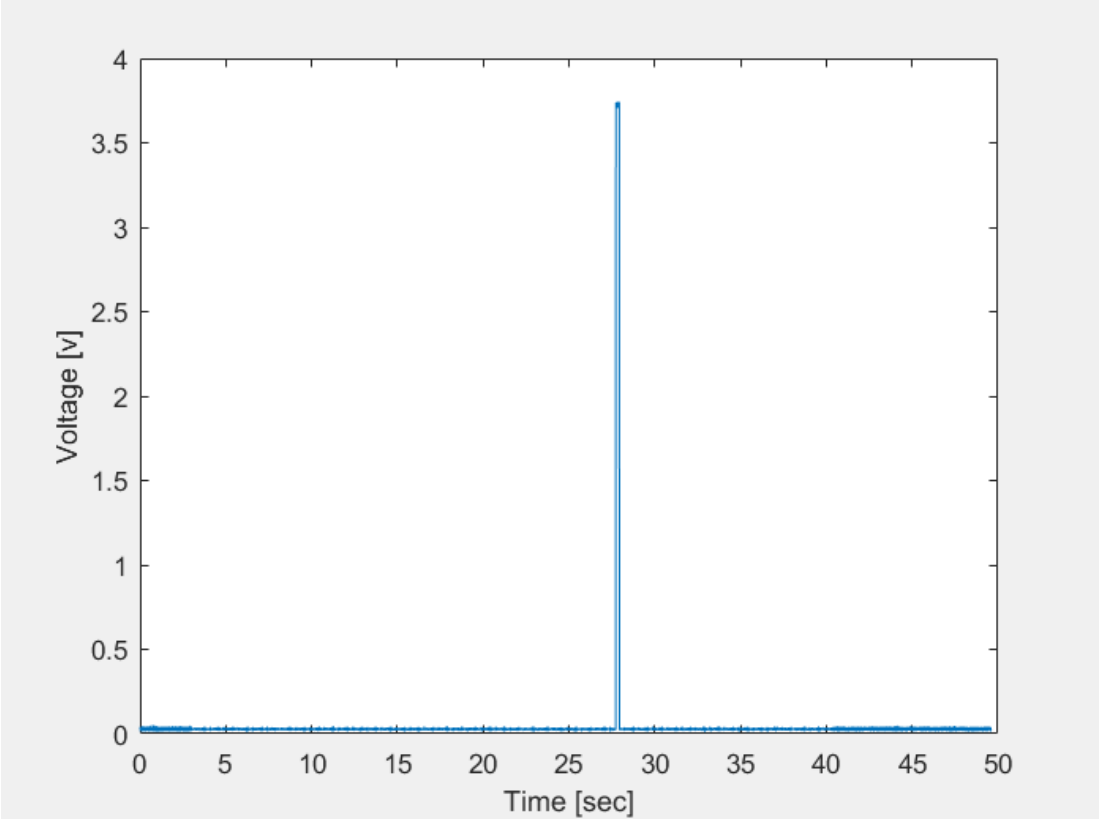

Figure 3.8.1: Trigger signal.

3.9 Particles

The flow was visualized using passive end neutrally buoyant tracing particles.
The tracing particles were microspheres, supplied by COSPHERIC, with a diameter between 180 and 212 μm and made by polyethylene with a density ρ_p of 1,22 g/cm^2.
Since Polyethylene is hydrophobic the microspheres needed to be coated with Tween 80 surfactant in order to avoid particles clothing.
The influence of the physical properties of particles on the fluid flow was estimated and resulted to be negligible. Indeed, the terminal velocity u_p acquired by the particles due to the Stokes's drag force, buoyancy and weight resulted to be 0.000166 m/sec. This value is two order of magnitude lower than the minimum mean magnitude velocity registered between the three geometries and for this reason was considered not effective. A more detailed guide about the estimation of the terminal velocity u_p can be found in Appendix A.5.

3.10 Illumination

The used visualization technique required an active lighting to provide an illumination of the seeded particles in the fluid.
To achieve a high particle contrast and therefore a high signal to noise ratio, a back light was used, in order to follow a shadowgraphy approach to visualize the particles.

3.11 Particles Tracks detection

As depicted in the mock loop scheme of Fig. 3.7.1 the PHOTRON-ultima video camera (high-speed camera N°1) was placed on the side of the phantom to have a perpendicular visual access into the sinus.
The diaphragm of PHOTRON-ultima video camera was fully closed[1] to obtain the entire region of interest in focus.
To obtain images with sufficient quality and contrast between the particles and the background the acquiring frame rate was set at 2000 images per second with an

[1] A closer diaphragm means deeper depth of focus, a more open diaphragm means a sharper depth of focus.

exposure time of 1/8000 s. These settings were chosen to have the highest frame rate maintaining the maximum resolution of the camera of 512 x 512 pixels.
Since the camera was placed perpendicularly at a known distance from the section test it was not necessary to fully calibrate it.
To compute the scaling from pixels to meters a calibration checkerboard was used. A more detailed guide about camera calibration can be found in Appendix A.6.
The total number of frames recorded by the PHOTRON-ultima video camera for each experiment was 2048. This last number correspond to a total recording period of 1.024 sec. Of this 2048 frames, only 1668 frames corresponding to 0.83 sec were taken into account for the analysis, since the heart rate was set at 72 bpm and only one pulse was analyzed for each experimental realization.
Examples of raw images acquired with the PHOTRON-ultima video camera are reported in the following Fig 3.11.1:

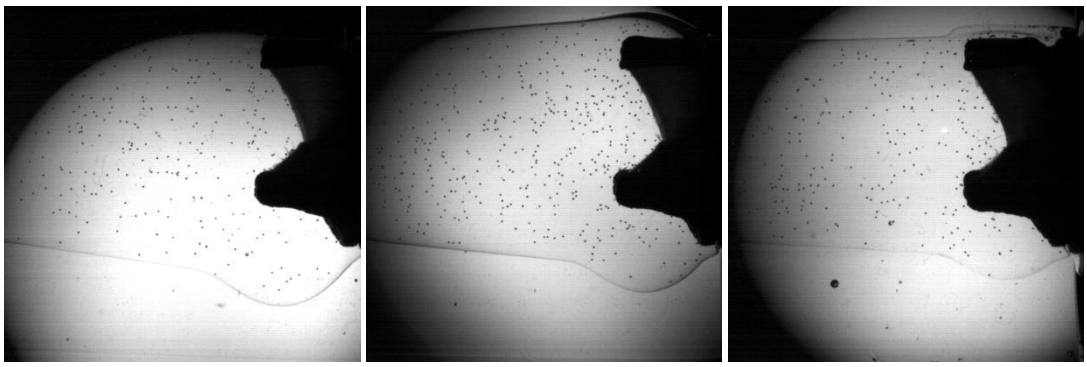

Figure 3.11.1: Raw images of the large geometry to the left, of the middle geometry in the middle and of the small geometry to the left.

To enhance the quality of the raw images an inversion of pixels intensity and a background removal was performed. In the following Fig 3.11.2 the computed backgrounds are reported.

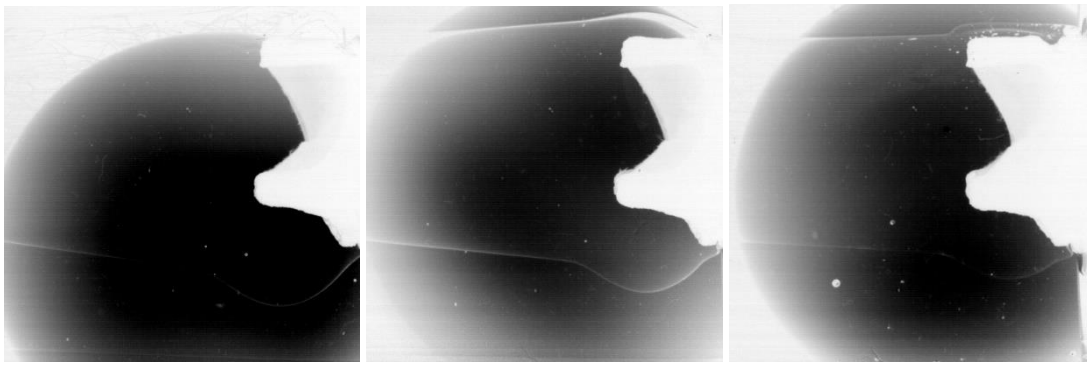

Figure 3.11.2: Background images of the large geometry to the left, of the middle geometry in the middle and of the small geometry to the left.

The background removal was implemented in such a way to erase from the images themselfs whatever did not change among a certain number of images. As can be seen in the matlab script compute_background.m reported in the Appendix A.11 this number was set to 500 images.
Below in Fig. 3.11.3 are reported the post processed images after the intensity inversion and background removal.

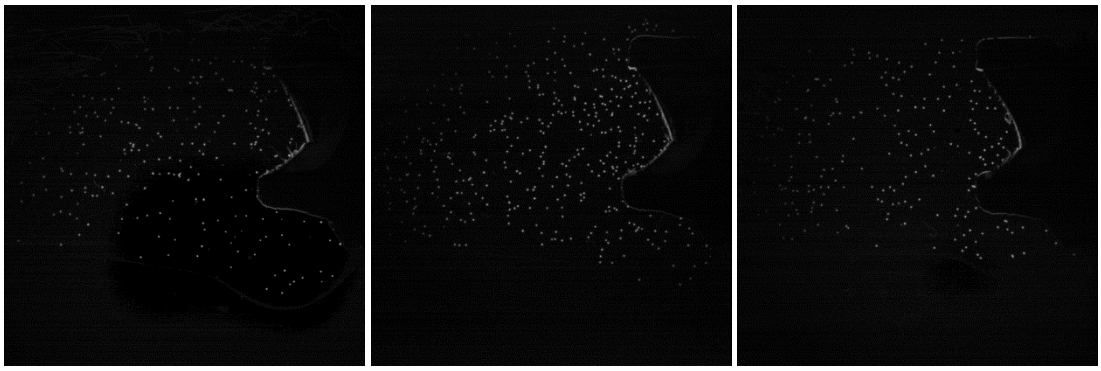

Figure 3.11.3: Post processed images of the large geometry to the left, of the middle geometry in the middle and of the small geometry to the left.

In other words, the post processed images reports whatever is moving during the recording. For this reason, in the sequences of post processed images, it was possible to clearly see the leaflets motion as showed in the following frames sequence of Fig.3.11.4.

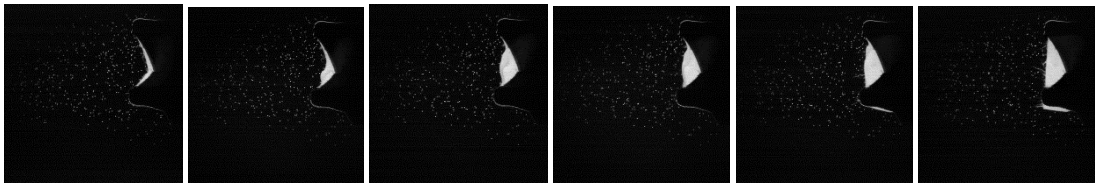

Figure 3.11.4: Post processed images sequence showing the leaflet movement.

The postprocessed images were then imported in ImageJ(Fiji) and two Region Of Interest (ROI) were defined.

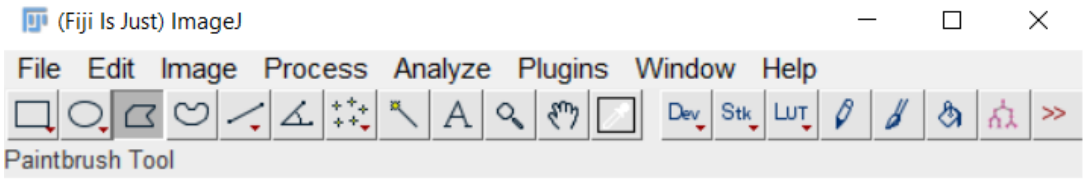

Figure 3.11.5: ImageJ (Fiji).

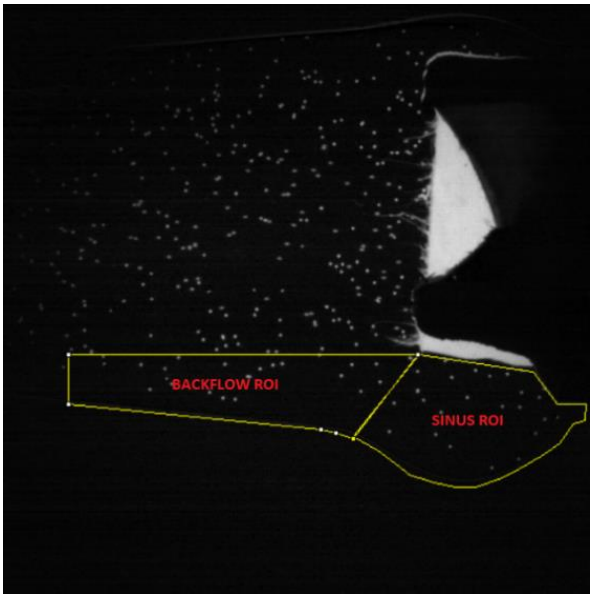

Figure 3.11.6: Backflow ROI and sinus ROI.

A first sinus ROI was drew in order to include the sinus region while a second backflow ROI was defined just downstream the sinus as reported in the Fig. 3.11.6 above.

Since the geometries of the silicon phantoms were different and also the position and rotation of the PHONTRON-video camera could have been slightly different among the experiments it was not possible to define an absolute ROI.
In order to make reproducible the drawing of the ROI among the realizations of the experiment few fixed geometrical referiment in the images were taken into account.
A more detailed guide about ROI definition can be found in Appendix A.7.
Two different tracks analysis were carried out with the plugings Track Mate of ImageJ (Fiji) for the two different ROI in focus.
A Linear Assignment Problem (LAP) was solved to track the particles in each analysis with the Linear motion LAP tracker of ImageJ (Fiji) [27].

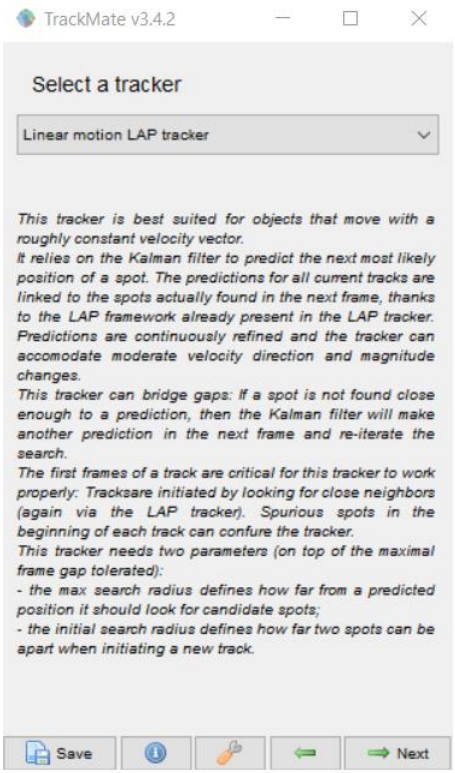

Figure 3.11.7: Linear motion LAP tracker of ImageJ (Fiji).

The Linear motion LAP tracker implemented in ImageJ (Fiji) relies on a Kalman filter to predict the most probable position of a particle undergoing constant velocity movement.

Tracks are initiated from the first two frames solving the Jaqaman cost matrix [28], that has as costs the square distances, with the Munkres & Kuhn algorithm [29]. The user can set what is the maximal distance allowed for the initial search with the Initial search radius setting.

Each track initiated from a pair of spots is used to create an instance of a Kalman filter. There are as many Kalman filters as tracks. In the next frames, each Kalman filter is used to generate a prediction of the most probable position of the particle. Then, all the predicted positions are linked against the actual spot positions in the frame, using again the Jaqaman LAP, with the square distance as costs. The user can set how far can be an actual position from a predicted position for linking with the Search radius setting.

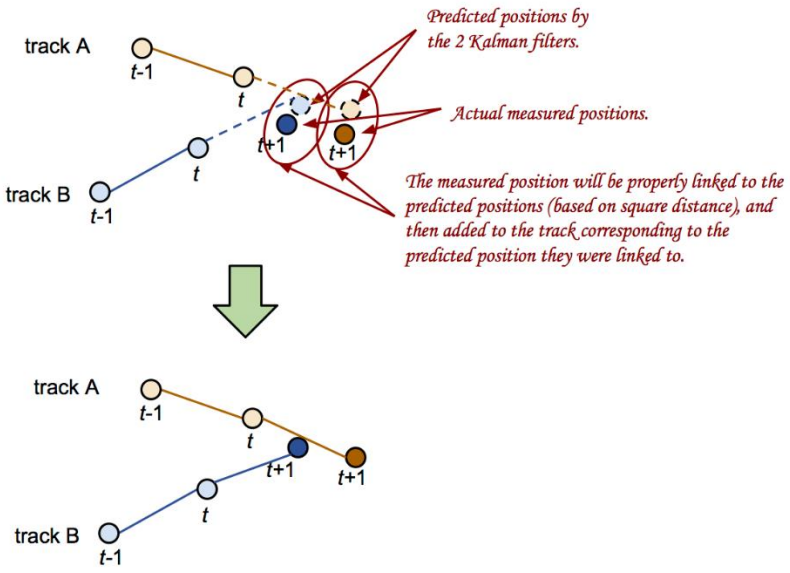

Figure 3.11.8: Fiji LAP working scheme (courtesy of [27]).

Some Kalman filters might not get linked to a found spot. This event is called an occlusion: the predicted position did not correspond to an actual measurement (spot). Kalman filters are still able to make a prediction for the next frame even with a missing detection. If the number of successive occlusions is too large, the track is considered terminated. The user can set the maximal number of successive occlusions allowed before a track is terminated with the Max frame gap setting.

Conversely, some spots might not get linked to a track. They will be used to initiate a new track in the next frame, as for the track initiation described above.
A more detailed guide about the Jaquaman LAP and Fiji LAP can be found in appendix A.8 and A.9 respectively.
In the following pictures of Fig. 3.11.9 and of Fig 3.11.10 are reported examples of the computed tracks with the above describe method.

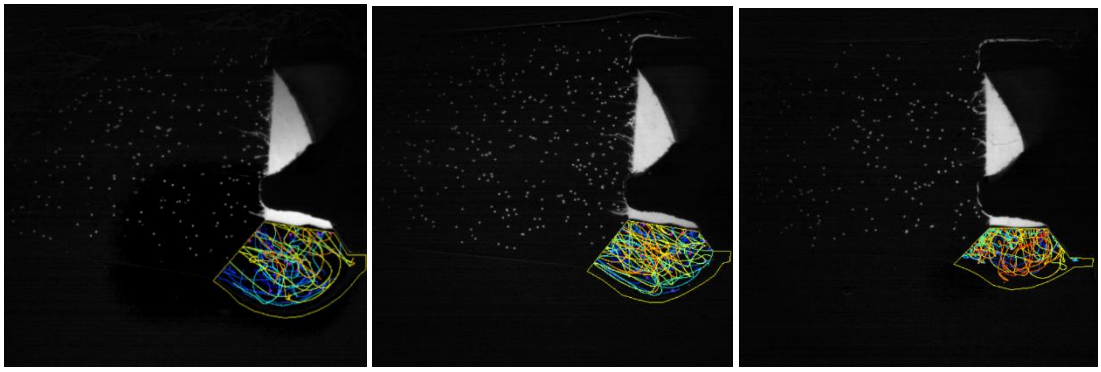

Figure 3.11.9: Computed tracks of the large geometry to the left, of the middle geometry in the middle and of the small geometry to the left for the sinus ROI.

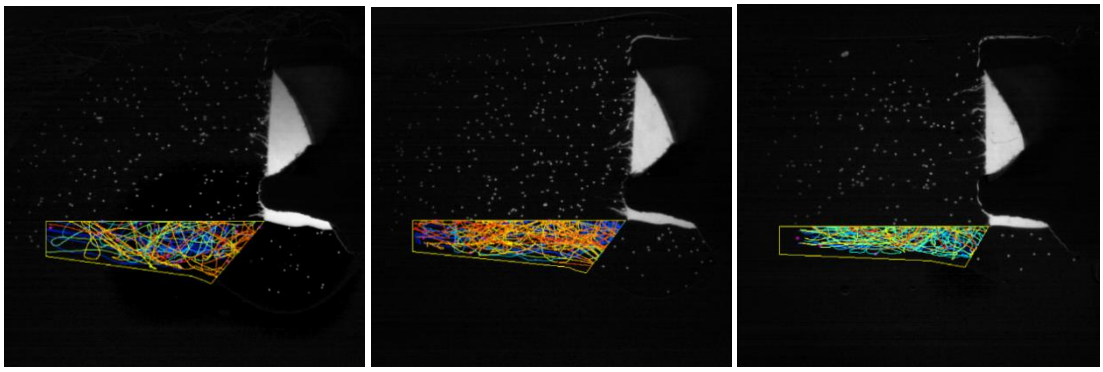

Figure 3.11.10: Computed tracks of the large geometry to the left, of the middle geometry in the middle and of the small geometry to the left for the backflow ROI.

All the experimental steps and the tracks exportation steps are summarized in the experimental protocol reported in the Appendix A.10 while the MATLAB scrip used for the preprocessing and post processing of the images are reported in the Appendix A.11.

3.12 Valve visualization

Images of the tested valve were acquired with the Jai TM-6740 GE CCD camera (camera N° 2 in Fig. 3.7.1). As can be seen in the figure 3.6, between the camera and the valve there was interposed the compliance chamber that however did not introduced any visual obstruction due to the transparency properties of Plexiglass.
The camera N° 2 was triggered with a signal generator activated in turn by an output signal coming from the piston pump. The maximum acquiring frame rate of the camera was 200 images per second so that a frequency of 200 Hz was used.

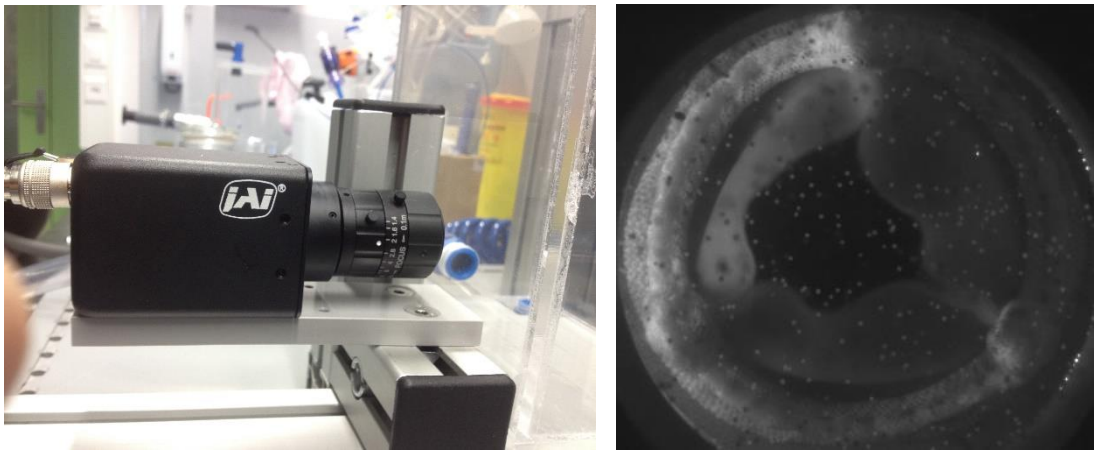

Figure 3.12.1: Jai camera to the left and an example of an acquired image to the right by itself.

4.RESULTS

4.1 Sinus region

In this chapter, the results regarding the sinus ROI of the three geometries are reported.

The following velocity histograms (Fig 4.1.1, Fig. 4.1.2, Fig. 4.1.3) show how the velocities of the particles in the sinus vary during the pulse. For every geometry, the velocity histogram of the U horizontal projected velocity component, the V vertical projected velocity component and the projected velocity magnitude M= $(U^2 + V^2)^{1/2}$ were computed. Hence, each velocity histogram represents the evolution of the three projected velocity components along the pulse.

On the x-axis is reported the velocity in m/s, on the y-axis the time in frames while the colours indicate the number of tracked particles in a certain frame with a specific velocity. The colour scale goes from blue to red, where blue indicates that the number of tracked particles showing a specific velocity is minimum in a certain frame while red indicates that the number of tracked particles exhibiting a specific velocity is maximum in a certain frame. In other words, the colours can be seen as intensity values of a third out of plane z-axis reporting the number of particles within a specific velocity bin in a certain frame. The colour bar is reported in the velocity histogram and refers to all the U, V and M velocity of the image. As can be seen from the script plot_tracks.m reported in the Appendix A.11 the total velocity range of U, V and M was divided in 35 bins.

In the velocity histograms of each geometry are reported the U, V and M velocities of all the tracks exported from all five-experimental realization and the mean of the velocity U, V and M over all the tracks exported from all five-experimental realization. It must be noted that negative values of U mean forward flow, while positive values mean backward flow. Positive values of V instead mean downward movement of particles while negative values mean upward movement of particles.
The values of U and V are contained in the interval from -0.3 m/s to +0,3 m/s while the velocity magnitude M is comprised between 0 and +0.3 m/s.
As can be seen in Fig. 4.1.1, 4.1.2 and 4.1.3, even if the morphology of the velocity histograms of the three different geometries are similar, the velocity ranges indicate a different behaviour of the tracked particles in the sinus during the pulse.
In all the geometries, approximately at the 200th frame a negative deviation in the U velocity component and a slightly positive peak in the M velocity magnitude can be recognized.
This event corresponds to the valve opening at early systole as can be verified from a direct observation to the post processed images.
In the three geometries in the first part of the pulse, the velocity distribution of U and V is contained in a narrow interval of velocities but around the 600th frame for the large and medium geometry, and around the 400th frame for the small geometry, it increases. Later in the pulse, round the 1000th frame the velocity distribution of U and V gets increasingly narrow for all the geometries. In the time interval comprise between the 600th frame and the 1000th frame the valve closing at late systole and the early diastole of the pulse are included. In this time span the U and V velocity ranges of the three geometries are different as confirmed by the velocity magnitude M. In particular, the U and V velocity range of the middle geometry is the biggest while the U and V velocity range of the small geometry is the smallest.
Looking at the M velocity magnitude histograms of the large and medium geometry it can be noted that the particles in the sinus acquire kinetic[2] energy and increase their velocity only at late systole. During early and middle systole indeed, the particles in the sinus have almost zero velocity magnitude even dough the central jet in the centre of the aortic root is already formed. The increment in the velocity magnitude at late systole is associated to a chaotic fluid dynamics that can be directly observed from the

[2] The kinetic energy is defined as $K = \frac{1}{2} * m * v^2 = \frac{1}{2} * m * M^2 = \frac{1}{2} * m * (U^2 + V^2)$.

post processed images. After valve closure, during diastole the velocity magnitude M gets increasingly closer to zero with an exponential decay typical of kinetic energy dissipation.

The velocity histogram referred to the small geometry reveals a similar overall fluid dynamics scenario except for a significant difference in the interval between the 400th frame and the 750th frame. In this interval, the velocities U and V vary with an oscillating pattern. This pattern could be the effect of the fluttering of the valve leaflets that can be seen from a direct observation of the post processed images.

Another difference that can be seen from the velocity histogram of the small geometry is that before and after the above discussed time intervals the velocity components U and V are collected in a narrower velocity range with respect to the ones of the large and medium geometry.

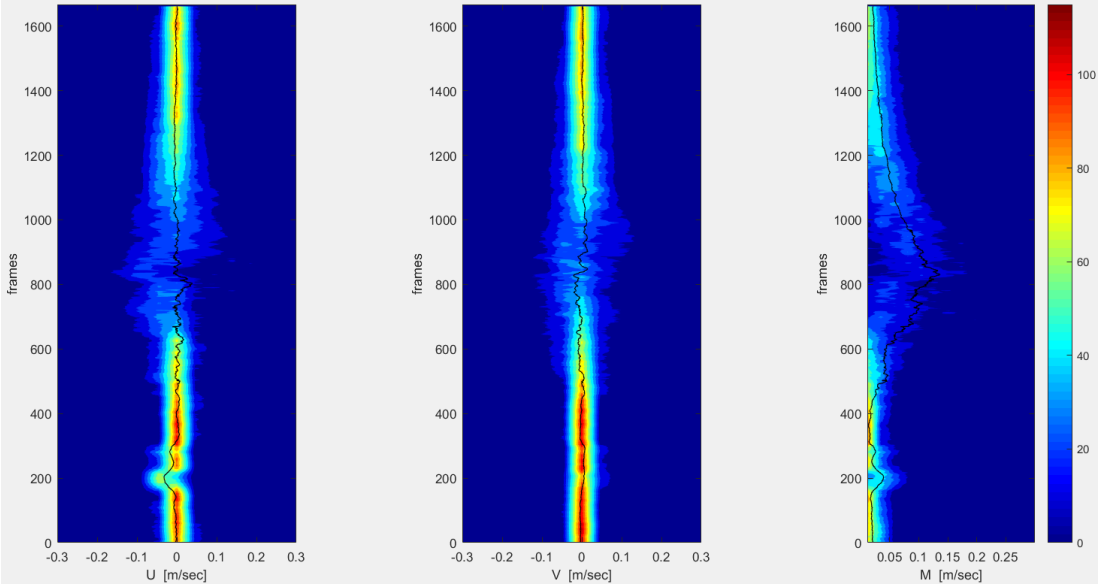

Figure 4.1.1: Velocity histogram of the large geometry.

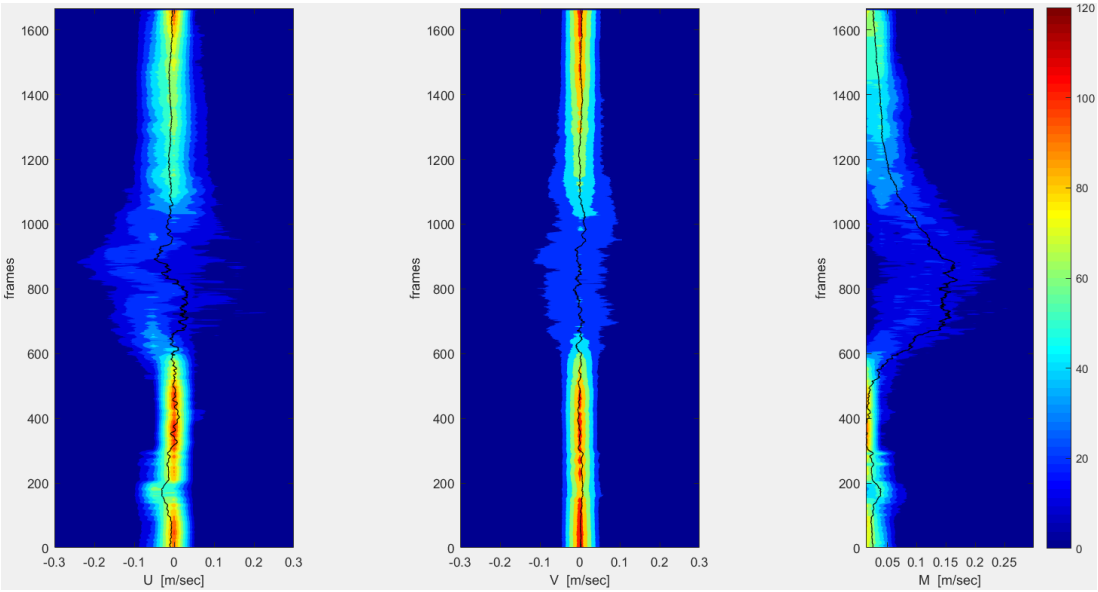

Figure 4.1.2: Velocity histogram of the middle geometry.

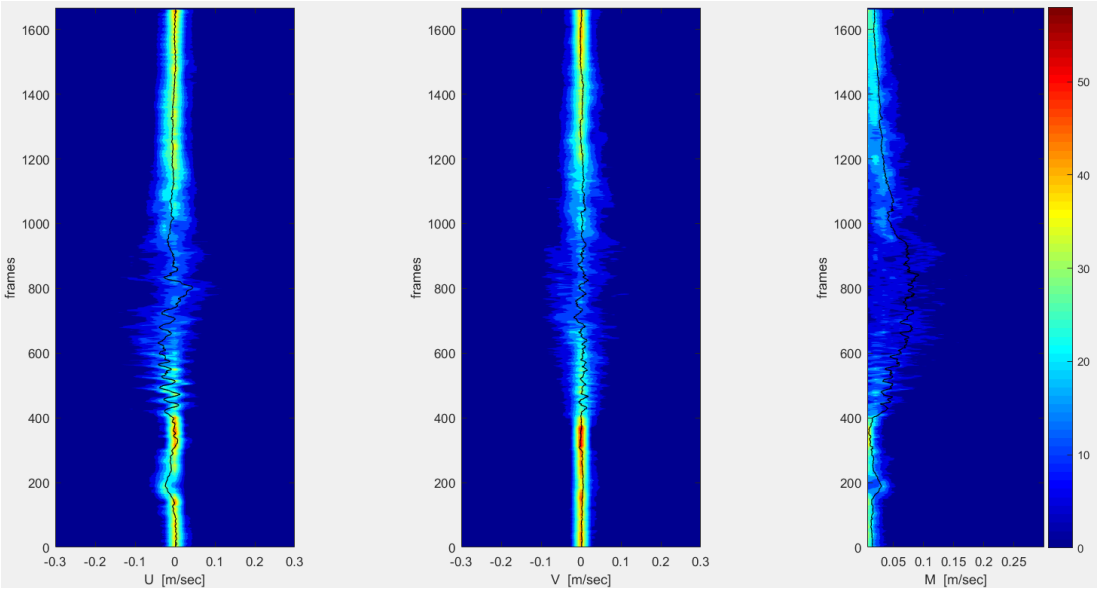

Figure 4.1.3: Velocity histogram of the small geometry.

What has been seen qualitatively from the velocity histograms and other properties extracted from the tracks analysis are quantitatively reported in the Table 4.1.1.

	Mean over the 5 experimental realizations of:	Units:	SMALL GEOMETRY	MEDIUM GEOMETRY	LARGE GEOMETRY
1st	Tracks	N°	100.80	202.40	167.00
2nd	In-in	%	0.37	0.11	0.00
3rd	In-out	%	11.40	13.83	14.67
4th	Out-in	%	13.32	13.24	13.80
5th	Out-out	%	74.90	72.82	71.53
6th	Resident time in-out	s	0.2387	0.2089	0.2532
7th	Std resident time in-out	s	0.1804	0.1532	0.1804
8th	U 650-950	m/s	-0.003	0.001	0.004
9th	Std U 650-950	m/s	0.043	0.095	0.070
10th	V 650-950	m/s	0.001	-0.002	-0.004
11th	Std V 650-950	m/s	0.043	0.066	0.051
12th	M 650-950	m/s	0.076	0.144	0.100
13th	Std M 650-950	m/s	0.051	0.092	0.072
14th	U 1200-1400	m/s	-0.005	-0.009	-0.005
15th	Std U 1200-1400	m/s	0.020	0.036	0.029
16th	V 1200-1400	m/s	0.001	0.002	0.004
17th	Std V 1200-1400	m/s	0.026	0.028	0.029
18th	M 1200-1400	m/s	0.030	0.041	0.035
19th	Std M 1200-1400	m/s	0.019	0.025	0.025

Table 4.1.1: Quantitative values computed for the three geometries.

In the following paragraphs where not specified, the wording “mean” must be interpreted as the mean over all the tracked particles of one experimental realization and all the discussed variables must be intended as mean over the five-experimental realization.

- In the 1st row of the table is reported the total number of detected particles. In the medium geometry, the number of tracked particles resulted to be the highest. It has to be noted that these values are strongly influenced by the seeding density of the particles into the RIM fluid that was hard to be

maintained constant because of particles accumulation in certain regions of the setup.

- In the 2nd row of the table is reported in percentage the number of particles that stayed in the ROI during the whole duration of the recording. The values resulted to be around 0 for all the three geometries.
- In the 3rd row of the table is reported in percentage the number of particles that were present in the ROI at the beginning of the recording and exited it during the pulse. The values resulted to be comparable for all three geometries.
- In the 4th row of the table is reported in percentage the number of particles that were not present in the ROI at the beginning of the recording but entered it later during the pulse. The values resulted to be comparable for all three geometries.
- In the 5th row of the table is reported in percentage the number of particles that were not present in the ROI at the beginning of the recording and exited it before the ending of the recording. For all the geometries in this group are contained the majority of the tracked particles.
- In the 6th row of the table is reported the mean resident time in seconds of the tracked particles that were inside the sinus ROI at the beginning of the recording and left it during the pulse. The shortest resident time was registered for the medium geometry while the large geometry showed the longest.
- In the 7th row of the table is reported the standard deviation in seconds of the mean resident time of the tracked particles that were inside the sinus ROI at the beginning of the recording and left it during the pulse.
- From the 8th to the 13th row of the table is reported the mean of U, V and M computed in the time frame interval [650 950] and the standard deviation of U, V and M computed in the time frame interval [650 950]. Looking at the standard deviations of U, V and M can be seen that the biggest values are associated with the medium geometry while the smallest values with the small geometry. The large geometry shows values between the other two geometries.
- From the 14th to the 19th row of the table is reported the mean of U, V and M computed in the time frame interval [1200 1400] and the standard deviation of U, V and M computed in the time frame interval [1200 1400]. Looking at

the standard deviations of U can be seen that the biggest values are related with the medium geometry while the smallest value with the small geometry. The large geometry shows a value between the other two geometries.

The time span [650 950] was focused with the aim to fully include the period when the distribution of the projected velocity U, V and M deviate from zero in all the geometries (from the 650th frame to the 950th frame) and exclude at the same time the period when the effect of the leaflet fluttering of the small geometry is predominant (from the 400th frame to the 750th frame). This time span as already mentioned is associated to a chaotic fluid dynamics that can be observed directly from the post processed images at late systole. The time span [1200 1400] was focused to analyse the U, V and M velocities of the three geometry during diastole after the chaotic fluid dynamics event at late systole.

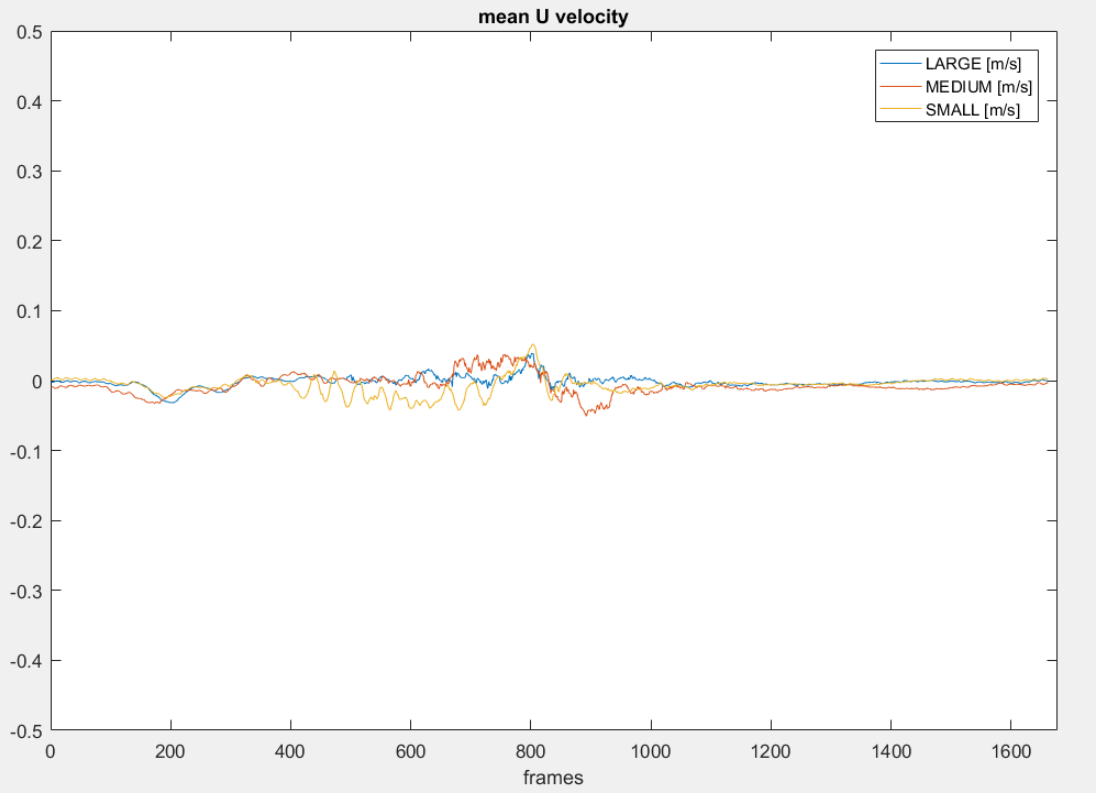

Figure 4.1.4: Mean horizontal velocity component U for the three geometries.

In the above reported Fig. 4.1.4 is reported the mean horizontal velocity component U for the three geometries. For all geometries, can be recognized a negative peak at valve opening (200th frame) and a positive peak corresponding to valve closure at the 800th frame. In the time span from the 400th frame until the 750th frame the large and medium geometry share a similar behavior while the small geometry shows the oscillating pattern noticed in the velocity histograms.
For all geometries, at valve closure (800th frame), the mean horizontal U velocity component inverts its sign, meaning that particles that were travelling backward at late systole (wash-in the sinus), just after valve closure start travelling forward (wash-out the sinus).

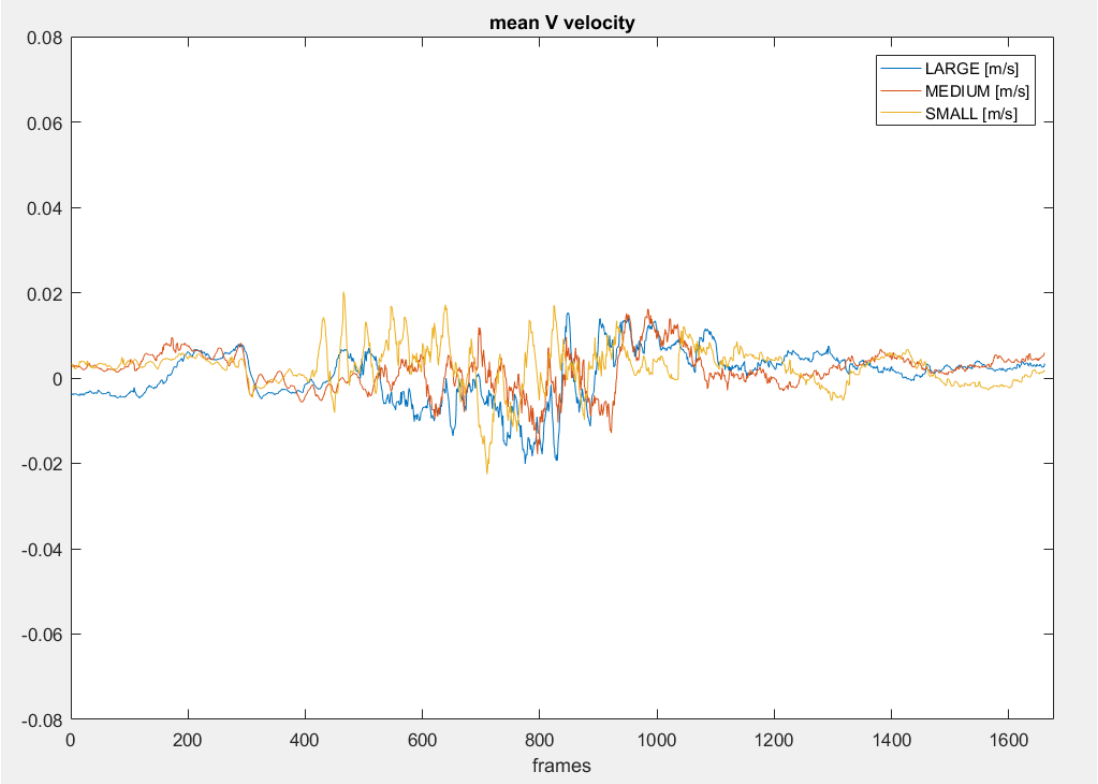

Figure 4.1.5: Mean vertical velocity component V for the three geometries.

The reading of the above reported Fig. 4.1.5 is more difficult because of the presence of large oscillation in the mean vertical velocity component V of all the three geometries. A positive peak at 200th frame and a negative peak at 800th frame, corresponding to the valve aperture and closure respectively, can still be recognized.

From the peaks present in V velocity component of the small geometry the oscillation frequency was computed as reported in the MATLAB script fluttering.m in Appendix A.11. The frequency of the oscillations was estimated to be around 40 Hz.

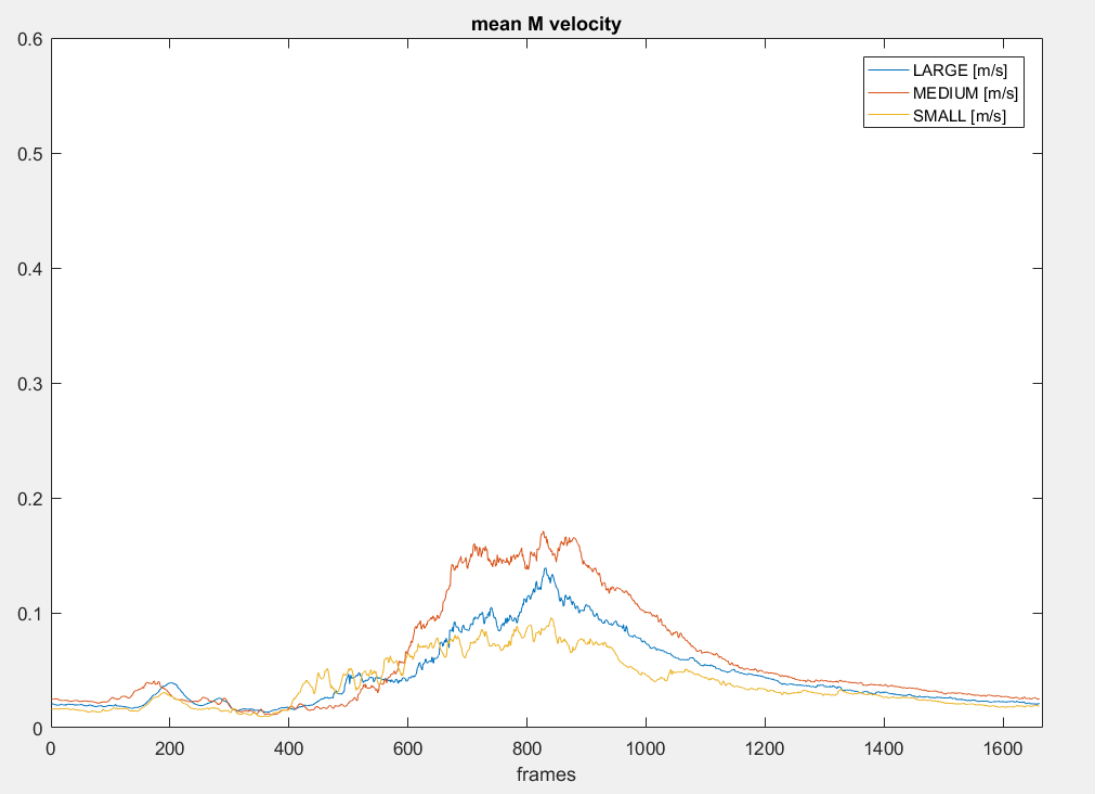

Figure 4.1.6: Mean velocity magnitude M for the three geometries.

The Fig. 4.1.6 showing the mean of the velocity magnitude M reveal that in the sinus ROI the particles in the medium geometry are faster with respect to the ones in the large and small geometry and that the particles in the small geometry are slower than the ones in the medium and large geometry. This observation is true during the whole duration of the pulse except in the time window between the 400th frame and the 650th frame where this hierarchy is not clear anymore. In this period the small geometry reveals higher velocity magnitude due to the leaflet fluttering.

4.2 Backflow region

In this chapter the results regarding the backflow ROI of all three geometries are reported. As for the sinus ROI, for each geometry, the velocities U, V and M are reported in velocity histograms (Fig. 4.2.1, 4.2.2 and 4.2.3) to collect all the tracks exported from all five-experimental realization. The values of U and V are contained in the interval from -0.8 m/s to +0.8 m/s while the velocity magnitude M is comprised between 0 and +0.8 m/s.

For all geometries in the first part of the pulse, the U velocity distribution is contained in a narrow interval and move towards negative values until the 300th frame. After the 300th frame the behaviour of the three geometries is different.

In the medium and large geometry, the U velocity distribution becomes wider and positive until the 950th frame when it gets narrower around 0. In the time interval between the 300th frame and the 950th frame the mid systole, the valve closing at late systole and the early diastole of the pulse is comprised. A positive U velocity component means that the tracked particles are moving from the region downstream the aortic root towards the sinus. This back flow is evident in the large and medium geometry and can be seen also in the small geometry but only during valve closure at the 800th frame.

Referring to the backflow period, the U velocity range of the middle geometry seem to be the biggest while the U velocity range of the small geometry seem to be the smallest. Despite of the presence of backflow close to valve closure at the 800th frame, the small geometry reveals a significant difference in the U velocity component in the interval comprise from the 300th frame to the 750th frame. In this interval, the U velocity component range is negative reviling a forward flow.

All M velocity magnitude histograms show that the particles in the backflow region acquire kinetic energy and increase their velocity just after the valve aperture. Until the 300th frame the acquired kinetic energy is related to a forward movement of particles in all the geometries. After the 300th frame the kinetic energy of the large and medium geometry is associated with the backward flow towards the sinus while the one of the small geometry with a forward flow. Looking directly to the post processed images can be seen that the backflow is generated by the fluid comprised between the central jet and the aortic root wall. The quantity of this fluid is affected by the geometry: is maximum in the large geometry and almost absent in the small geometry.

In the small geometry indeed, the central jet engages the aortic root just after the valve without leaving room to host the backflow fluid.

In the medium geometry, despite a lower quantity of fluid available between the central jet and the aortic wall with respect to the one of the large geometry, the fastest back flow was registered. After valve closure during diastole, the velocity magnitude M gets increasingly closer to zero with an exponential decay typical of kinetic energy dissipation in all geometries.

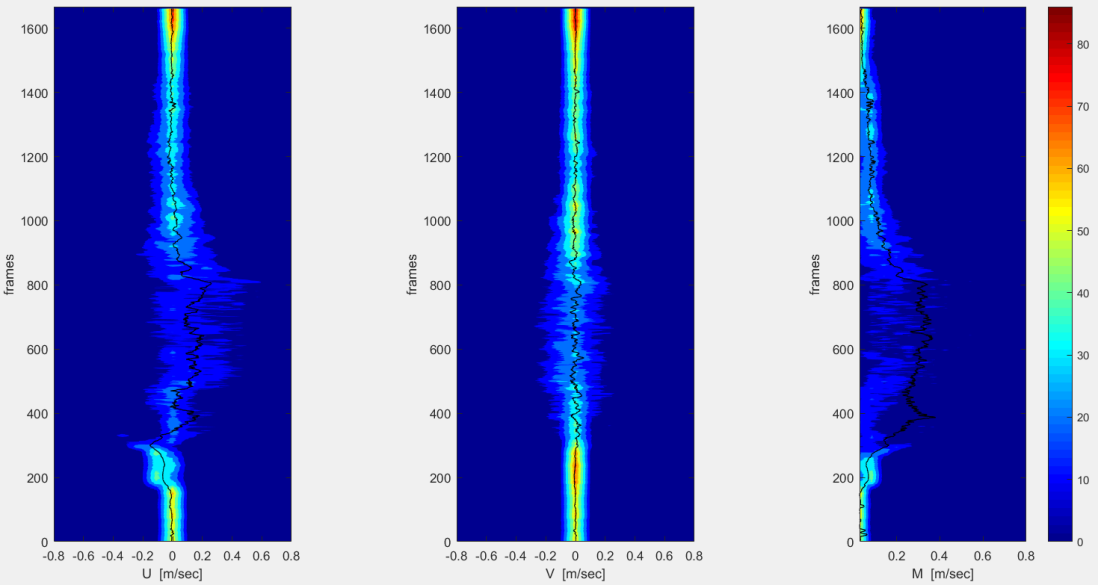

Figure 4.2.1: Velocity histogram of the large geometry.

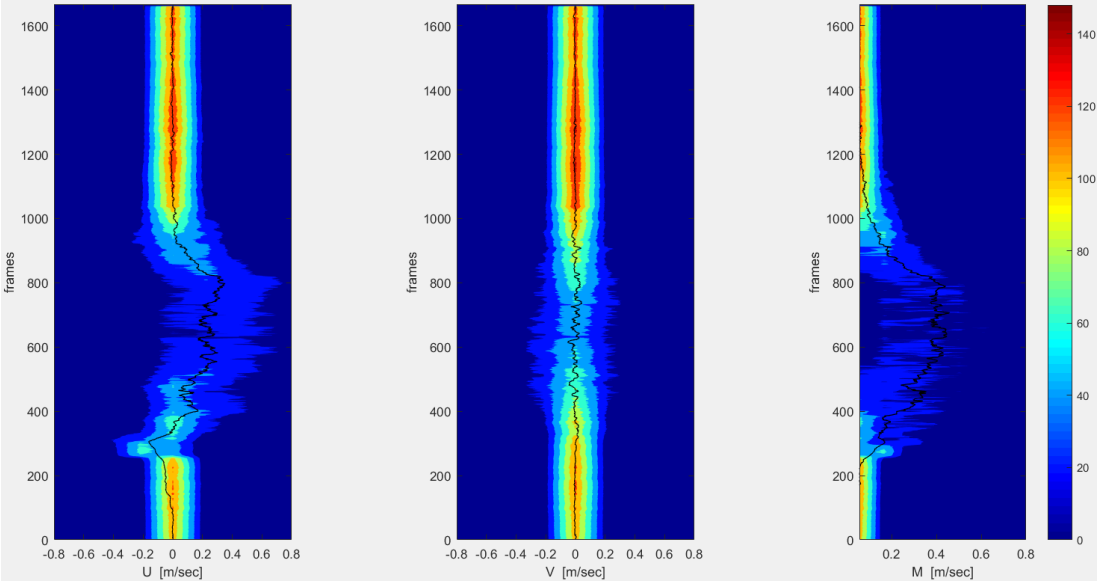

Figure 4.2.2: Velocity histogram of the middle geometry.

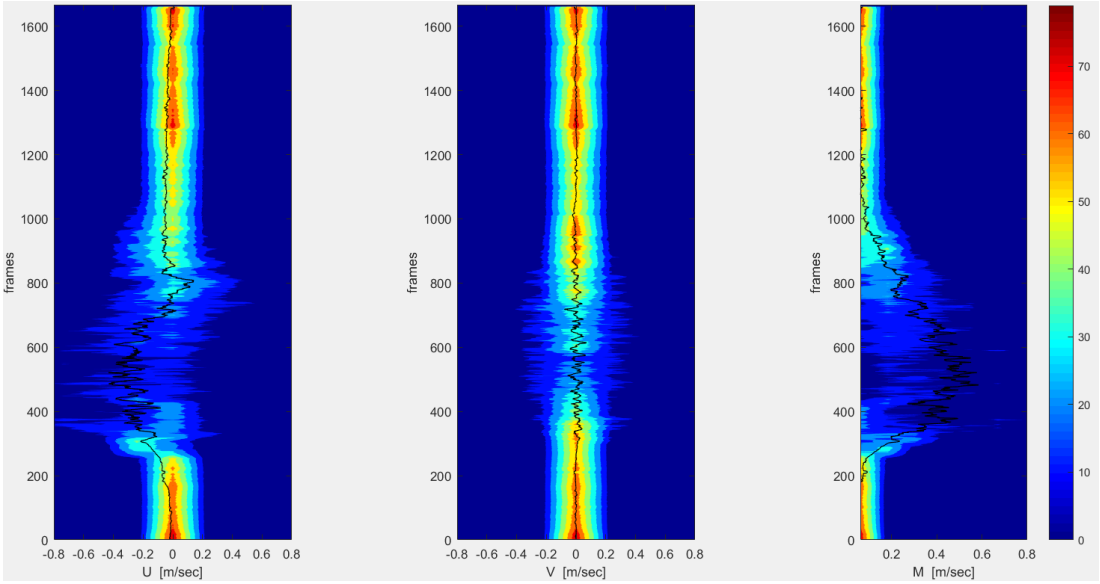

Figure 4.2.3: Velocity histogram of the small geometry.

What has been seen qualitatively from the velocity histograms and other properties extracted from the analysis are quantitatively reported in the Table 4.2.1.

	Mean over the 5 experimental realizations of:	Units:	SMALL GEOMETRY	MEDIUM GEOMETRY	LARGE GEOMETRY
1st	Tracks	N°	225	354.20	265.60
2nd	In-in	%	0.00	0.00	0.00
3rd	In-out	%	7.14	6.28	5.13
4th	Out-in	%	6.91	7.049	6.35
5th	Out-out	%	85.95	86.67	88.51
6th	U 400-950	m/s	-0.093	0.154	0.105
7th	Std U 400-950	m/s	0.234	0.214	0.191
8th	V 400-950	m/s	-0.009	-0.001	-0.002
9th	Std V 400-950	m/s	0.122	0.125	0.119
10th	M 400-950	m/s	0.331	0.339	0.273
11th	Std M 400-950	m/s	0.226	0.198	0.177
12th	U 1200-1400	m/s	-0.040	-0.003	-0.007
13th	Std U 1200-1400	m/s	0.044	0.055	0.063
14th	V 1200-1400	m/s	0.002	-0.005	-0.0004
15th	Std V 1200-1400	m/s	0.027	0.032	0.049
16th	M 1200-1400	m/s	0.057	0.054	0.075
17th	Std M 1200-1400	m/s	0.036	0.038	0.043

Table 4.2.1: Quantitative values computed for the three geometries.

For the analysis of the backflow region the same parameters of the sinus region were considered with the only difference that the time intervals taken into account to compute the mean velocities U, V, M and their standard deviations are the time spans [400 950] and [1200 1400]. The time span [400 950] was selected with the aim to fully include the back flows of all the three geometries and focus the analysis on them. The time span [1200 1400] was focused to analyse the U, V and M velocities after that the backflow was extinguished.
The resident time and its standard deviation were not computed.
The values reported in the Table 4.2.1 and the below discussed quantities have to be interpreted as specified in the previous chapter.

In the 6th row of the table is reported the mean U velocity computed in the time frame interval [400 950]. In this time span the backflow of the three geometry should be contained but the computed mean U velocity of the small geometry is negative. This happens because the backflow of the small geometry is present only at valve closure and it is not visible anymore ones that the mean is made over the whole-time span from the 400th frame and the 950th frame.
Comparing the medium and the large geometry, the first one shows a bigger positive value of U meaning a faster backflow.

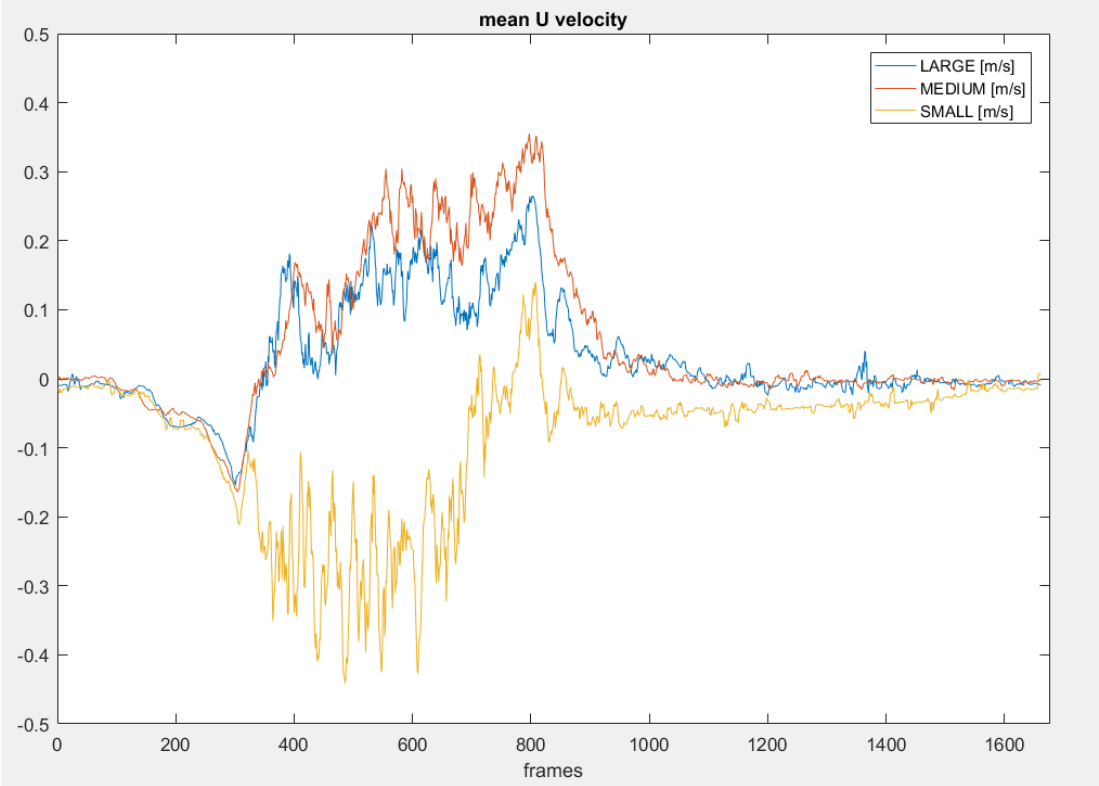

Figure 4.2.4: Mean horizontal velocity component U for the three geometries.

In Fig. 4.2.4 is reported the mean horizontal velocity component U for the three geometries. In all the three geometries, can be recognized a positive peak in correspondence of the valve closure at the 800th. From the 300th frame until valve closure the large and medium geometry share a similar behavior with positive backflow velocities while the small geometry shows a negative forward flow velocity.

During valve closure at the 800th frame, also the mean horizontal U velocity component of the small geometry inverts and become positive.
Around valve closure the medium geometry has the fastest backflow, the small geometry the slowest while the one of the large geometry is in between.
Correlating the U velocity graphs of the two analyzed ROI can be seen that the backflow peak at the 800th frame in the Fig.4.2.4 is associated to the backward flow peak at the 800th frame of Fig.41.4. Indeed, to generate the backward flow in the sinus ROI is the backflow coming from the backflow ROI as can also be seen from a direct observation of the post processed images.

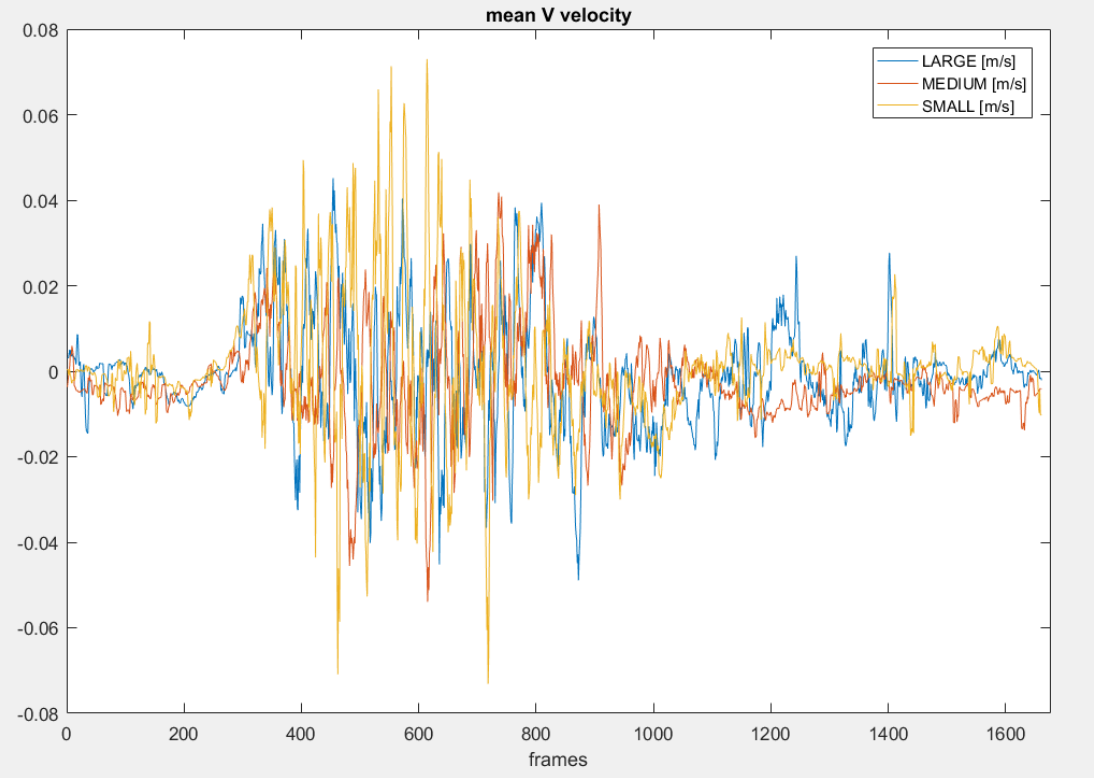

Figure 4.2.5: Mean vertical velocity component V for the three geometries.

As for the sinus ROI, it is hard to read the graph related to the mean vertical velocity component V (Fig. 4.2.5) because of the chaotic movement of particles.

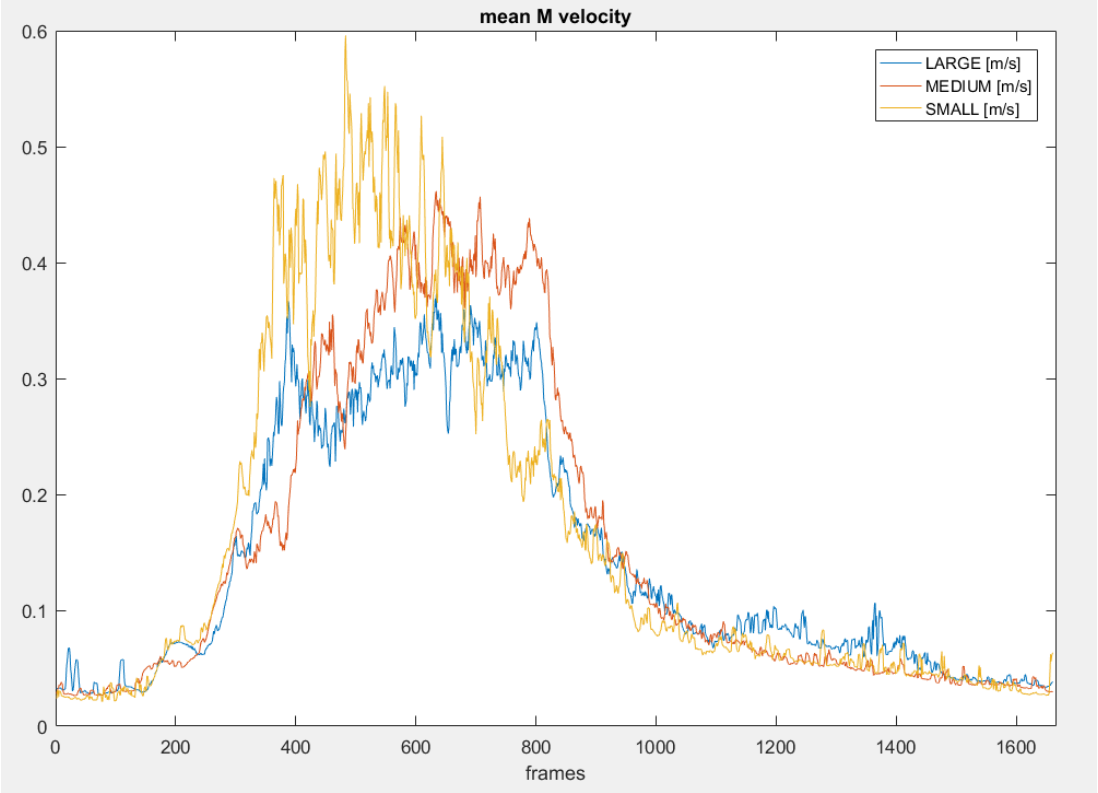

Figure 4.2.6: Mean velocity magnitude M for the three geometries.

Fig. 4.2.6 shows that the mean of the velocity magnitude M of the small geometry is the highest until valve closure when it becomes the smallest. Around the 800th frame indeed the highest value of mean velocity magnitude M is related to the middle geometry. As better understandable form the U velocity component, this time span is associated with the backward flow meaning that the medium phantom has the fastest backflow and the small phantom the slowest one.

5.DISCUSSION AND CONCLUSIONS

5.1 The fluid dynamics in the aortic root

The fluid dynamics in the aortic root is strongly 3-dimensional and unsteady. Measuring the 3-dimensional field in a time resolved manner is an out most challenging task. On the other hand, 2-dimensional investigation is much easier to perform and can help to understand the fundamental events that are taking place in the aortic root during the heart pulse.

The overall fluid dynamics behaviour of the three geometries can be extracted from the PTV analysis of the two ROI and from the direct observation of the post processed images.

In the sinus ROI, the analysis of the tracks in the medium and large geometry showed that at the beginning of the heart pulse the particles have low velocity until late systole when their motion become stronger. The particles move at higher velocities until mid-diastole. In the small geometry, the particles gain velocity earlier (from the 400th frame) due to the leaflet fluttering.

In all geometries, at valve closure (800th frame) The U velocity component inverts from a positive backward flow to a negative forward flow (Fig.4.1.1, Fig.4.1.2, Fig.4.1.3 Fig.4.1.4).

In the backflow ROI, at valve closure (800th frame) the analysis of the tracks in all geometries showed that close to the aortic wall the particles travel backward towards the sinus. This backflow is present from the 300th frame in the large and medium geometry but can only be seen close to valve closure in the small geometry.

At valve closure (800th frame) The U velocity components reaches a positive backflow peak for all the three geometries (Fig.4.2.1, Fig.4.2.2, Fig.4.2.3 Fig.4.2.4).

Combinig this findings with the direct observation of the post processed images the following overall fluid dynamics behaviour for the medium and large geometry can be hypothesized:

- valve aperture at 200th frame;
- development of the central jet with the ASV advected away along the aortic root between the 200th frame and the 400th frame;
- creation of a backflow region close to the aortic wall downstream the sinus between the 400th frame and the 600th frame. The back-flow fluid in this period mainly flows back into the central jet and does not enter the sinus where the fluid remains stagnant with almost zero velocity until late systole (600th frame);
- developed central jet and back flow separated by a shear layer from the 600th frame until valve closure at 800th frame. The back-flow fluid in this period mainly enters the sinus increasing the motion of the fluid in it (Fig. 5.1.1);
- after valve closure the central jet disappears in the core of the aortic root while in the sinus, due to inertia, the fluid still move chaotically until the 1000th frame;
- progressive dissipation of the kinetic energy associated with chaotic motion of the fluid in the whole aortic root until the end of the pulse.

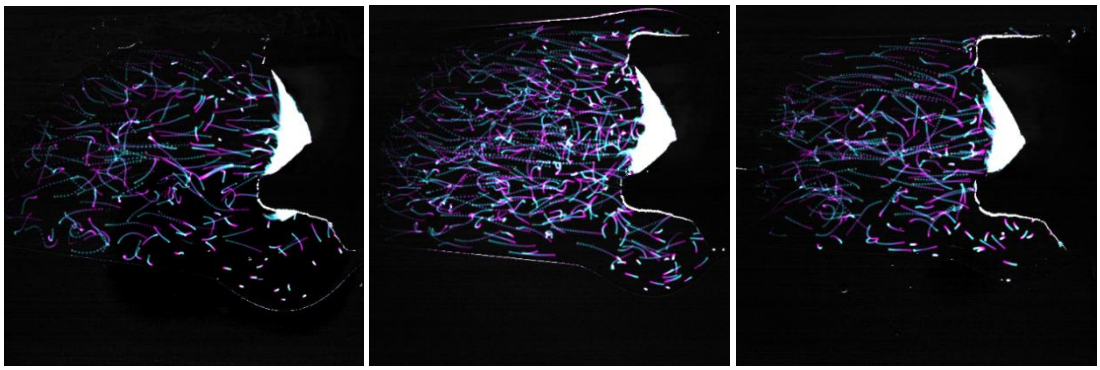

Figure 5.1.1: Tracks of a particles for the time span [780 800] for the large geometry to the left, the medium geometry in the middle and the small geometry to the right.

The above reported images show the movement of the particles from the frame 780th to the frame 800th. The colour of the tracks indicates the temporal evolution of the particles movement: light blue indicates older frames while violet indicates newer frames. In this time span it is possible to visualize particles travelling backward towards the sinus in all the three geometries close to the aortic root wall.
The images were produced with the MATLAB script particles_tracks.m reported in the Appendix A.11.
Referring to the literature cited in the Background section it was possible to recognize by eye in the sequence of post processed images of the large and medium geometry the initial counter clockwise ASV. In any geometry could be observed a clock wise sinus vortex of the type described by D.Moore and at. al [19]. This can be due to the different experimental condition and to the different geometry considered to mimic the aortic root.
In the sinus ROI instead of a structured clock wise vortex, a chaotic movement of fluid generated by the backward flow coming from the backflow ROI was observed at late systole and early diastole in all geometries.
Nevertheless, during valve closure at the 800th frame, the mean horizontal U velocity component inverts its sign in all geometries from positive to negative. That could mean that particles that were travelling backward at late systole, just after valve closure at the 800th frame invert their direction and start travelling forward. This can be interpreted as a hint for a wash out event.
Evidence of a backflow close to the aortic wall was already found in the works of D. Hasler et al. [25], and in the master thesis of D.Schimd 2016, ARTORG Center for Biomedical Engineering [26].
Further 3-dimensional fluid dynamics investigation are necessary to assess the behaviour of the backflow after having entered the sinus and its asymmetry. Indeed, the question that follows from the above fluid dynamics interpretation is where the backflow fluid goes after having entered the sinus region to respect the conservation of mass.
In the experimental set up as employed, the valve commissures were not connected to the aortic wall so that the fluid could flow also in the circumferential direction behind the valve commissures. The 2D PTV analysis as it was performed was not able to detect this circumferential motion of fluid. Evidence of the presence of this

circumferential flow was seen in the preliminary experiments. The circumferential flow seemed to be generated by the backflow entering the sinus and flowing behind the valve commissures in circumferential direction.
After flowing around the valve the circumferential backflow fluid seemed to come back in the central jet respecting the conservation of mass.
Further 3-dimensional analysis are necessary to confirm this overall fluid dynamics hypothesis and to investigate the non-symmetrical properties of the fluid dynamics in the aortic root.

5.2 The influence of the aortic root geometry

For what we have seen so far, the different size of the aortic root reflects different results of the PTV analysis in both the two considered ROI : the three geometries showed different fluid dynamics features in the sinus flow and in the backflow.
In the backflow ROI, the fastest backward flow was registered in the medium geometry, the slowest in the small geometry and the medium one in the large geometry (Fig. 4.2.4).
In Fig. 4.2.4 can be seen that the backflow of the medium and large geometry started after the 300th frame and reached its peak at valve closure. In the small geometry, the backflow was present only close to valve closure (800th frame).
The aortic root geometry determined the quantity of fluid available to generate the backward flow towards the sinus.
The large geometry had the bigger room between the central jet and the aortic wall of the phantom to host the backflow fluid while the small geometry had the smallest one.
The central jet in the small geometry, after valve opening, engaged the aortic wall just downstream the sinotubular junction without leaving any space for the backflow to form. This can be the reason why in the small geometry the backflow is not present from 300th frame but it appears only at late systole, close to valve closure, when the central jet is disappearing.
Even though the large geometry had the biggest space available for the backflow fluid the fastest backflow was registered in the medium geometry. This evidence could be

explained in light of a bigger area available for the backward fluid in the large geometry with respect to the one of the medium geometry[3].
The backflow in all geometries seem to be the most important factor for the increment of the kinetic energy in the sinus ROI at late systole as showed by the post processed images.
In the sinus ROI, the medium geometry showed an overall higher velocity magnitude associated with a higher kinematic energy (Fig.4.1.6). It could be argued that the higher kinetic energy acquired by the fluid at late systole due to the backward flow coming from the backflow ROI is related with a more efficient wash out.
To support this hypothesis, looking at the 6th row of Table 4.1.1, can be seen that the mean resident time of the medium geometry is the smallest between all geometries.
For what concern the other two geometries, the mean resident time of the large geometry is bigger than the one of the small geometry (Table 4.1.1).
As before, it could be argued that the wash out of the small geometry is more efficient than the one of the large geometry.
In this case however, the Fig.4.1.6 displays that the mean M velocity magnitude of the small geometry is higher than the one of the large geometry only between the 400th frame and the 750th frame when the fluttering od the valve was registered. In this case, the more efficient washout due to the increment of kinetic energy could be the effect of the leaflet fluttering more than the consequence of the backward flow coming from the backflow ROI that is present only close to valve closure.

5.3 Conclusion and future work

As predicted from the cited literature in the Background section it is possible to state that the fluid dynamics in the aortic root is influenced by the geometry.
Specifically, an oversized aortic root and an undersized aortic root are associated with slower backflows towards the sinus and lower kinematic energy in the sinus.
Further investigations are needed to access which fluid dynamics condition is preferable to avoid prosthetic heart valve thrombosis. Indeed, even if bigger quantities of kinetic energy could be associated with a more efficient wash out reducing the

[3] $Q = v * A$: if the prescribed flowrate is the same in a smaller section the fluid is faster and in a bigger section the fluid is slower.

stagnation of the blood in the sinus, higher velocity magnitude could also be associate with higher shear stresses and blood damage.
Further 3D investigations are necessary also to complete the 2D fluid dynamics picture which is described here.

BIBLIOGRAPHY

Bibliography

[1] M. Lengyel *et al.*, "Guidelines for management of left-sided prosthetic valve thrombosis: A role for thrombolytic therapy," *J. Am. Coll. Cardiol.*, vol. 30, no. 6, pp. 1521–1526, 1997.

[2] F. M. Cáceres-Lóriga, H. Pérez-López, J. Santos-Gracia, and K. Morlans-Hernandez, "Prosthetic heart valve thrombosis: Pathogenesis, diagnosis and management," *Int. J. Cardiol.*, vol. 110, no. 1, pp. 1–6, 2006.

[3] G. D. Dangas, J. I. Weitz, G. Giustino, R. Makkar, and R. Mehran, "THE PRESENT AND FUTURE Prosthetic Heart Valve Thrombosis," 2016.

[4] "Heart Valves." [Online]. Available: https://joinjj.com/heart-murmur-and-exercise/.

[5] "Aortic Valve." [Online]. Available: https://www.northwell.edu/sites/northwell/files/heart-anatomy-illustration.jpg.

[6] "Cardiac Cycle." [Online]. Available: https://upload.wikimedia.org/wikipedia/commons/9/9a/Wiggers_Diagram.png.

[7] F. Sotiropoulos, T. B. Le, and A. Gilmanov, "Fluid Mechanics of Heart Valves and Their Replacements," *Annu. Rev. Fluid Mech.*, vol. 48, no. 1, pp. 259–283, 2016.

[8] A. P. Yoganathan, K. B. Chandran, F. Sotiropoulos, and W. H. Coulter, "Flow in Prosthetic Heart Valves: State-of-the-Art and Future Directions," *Ann. Biomed. Eng.*, vol. 33, no. 12, pp. 1689–1694, 2005.

[9] N. Dü *et al.*, "Prosthetic valve thrombosis: Twenty-year experience at the Montreal Heart Institute."

[10] M. Higashidate, K. Tamiya, T. Beppu, and Y. Imai, "Regulation of the aortic valve opening. In vivo dynamic measurement of aortic valve orifice area," *J. Thorac.*

Cardiovasc. Surg., vol. 110, no. 2, pp. 496–503, 1995.

[11] G. Pisani *et al.*, "Role of the sinuses of Valsalva on the opening of the aortic valve," *J. Thorac. Cardiovasc. Surg.*, vol. 145, no. 4, pp. 999–1003, 2013.

[12] A. Salica *et al.*, "The combined role of sinuses of Valsalva and flow pulsatility improves energy loss of the aortic valve," *Eur. J. Cardio-thoracic Surg.*, vol. 49, no. 4, pp. 1222–1227, 2016.

[13] M. Gharib, D. Kremers, M. M. Koochesfahani, and M. Kemp, "Leonardo ' s vision of flow visualization," *Exp. Fluids*, vol. 33, no. 1, pp. 219–223, 2002.

[14] B. J. Bellhouse and L. Talbot, "Fluid mechanics of the aortic valve.," *Br. Heart J.*, vol. 31, no. 3, p. 391, 1969.

[15] B. J. Bellhouse, "Velocity and pressure distributions in the aortic valve," *J. Fluid Mech.*, vol. 37, no. 3, p. 587, 1969.

[16] R. Toninato, J. Salmon, F. M. Susin, A. Ducci, and G. Burriesci, "Physiological vortices in the sinuses of Valsalva: an in vitro approach for bio-prosthetic valves," *J. Biomech.*, pp. 1–9, 2016.

[17] G. Querzoli, S. Fortini, S. Espa, and S. Melchionna, "A laboratory model of the aortic root flow including the coronary arteries," *Exp. Fluids*, vol. 57, no. 8, pp. 1–9, 2016.

[18] J. P. Escobar Kvitting, T. Ebbers, L. Wigström, J. Engvall, C. L. Olin, and A. F. Bolger, "Flow patterns in the aortic root and the aorta studied with time-resolved, 3-dimensional, phase-contrast magnetic resonance imaging: Implications for aortic valve-sparing surgery," *J. Thorac. Cardiovasc. Surg.*, vol. 127, no. 6, pp. 1602–1607, 2004.

[19] B. Moore and L. P. Dasi, "Spatiotemporal complexity of the aortic sinus vortex," *Exp. Fluids*, vol. 55, no. 7, 2014.

[20] David Hasler, Bernhard Vennemann, Stefan Stortecky, Thomas Pilgrim, "HVS - Under What Conditions Do We Find Vortical Flow in the Sinus of Valsalva?" [Online]. Available: http://heartvalvesociety.org/meeting/abstracts/2017/A73.cgi.

[21] B. Soediono, *Particle Image Velocimetry*, vol. 53. 1989.

[22] R. Haj-Ali, G. Marom, S. Ben Zekry, M. Rosenfeld, and E. Raanani, "A general three-dimensional parametric geometry of the native aortic valve and root for biomechanical modeling," *J. Biomech.*, vol. 45, no. 14, pp. 2392–2397, 2012.

[23] W. M. SWANSON and R. E. CLARK, "Dimensions and Geometric Relationships of the Human Aortic Value as a Function of Pressure," *Circ. Res.*, vol. 35, no. 6, pp. 871–882, 1974.

[24] T. H. E. Geometry, O. F. The, A. Root, I. N. Health, A. V. Replacement, and A. T. Valve, "Technical Note the Geometry of the Aortic Root in Health ," no. June, 1989.

[25] D. Hasler, A. Landolt, and D. Obrist, "Tomographic PIV behind a prosthetic heart valve," *Exp. Fluids*, vol. 57, no. 5, pp. 1–13, 2016.

[26] D. S. Schmid, “Influence of the Sinus of Valsalva on the three-dimensional flow field behind a prosthetic valve by,” no. August, 2016.

[27] “TrackMate Algorithms - ImageJ.” [Online]. Available: http://imagej.net/TrackMate_Algorithms#cite_note-3.

[28] K. Jaqaman *et al.*, “Robust single-particle tracking in live-cell time-lapse sequences.”

[29] J. Munkres, “Algorithms for the Assignment and Transportation Problems,” *J. Soc. Ind. Appl. Math.*, vol. Vol.5, pp. 32–38.

APPENDIX

Appendix

A.1 Geometrical parameters relationships

The following geometrical relationship were used to make the constructive dimension r_m and r_v only function of α_{co} and α_s :

$$r_{co} = \alpha_{co} r_r \qquad (1)$$

$$r_v + r_m = r_s = \alpha_s r_r \qquad (2)$$

$$r_v^2 = r_{co}^2 + r_m^2 - 2 r_{co} r_m \cos 60° \qquad (3)$$

From the following drawing of Fig. A.1.1 is trivial to visualize the meaning of the equation (1) and (2) while equation (3) expresses the Carnot Theorem[4] for the triangle underlined in red.

[4] Carnot Theorem: in any triangle, the measure of each squared side is equal to the sum of the measures of the other two sides squared minus twice the product of the two measures of the two sides times the cosine of the angle included therebetween.

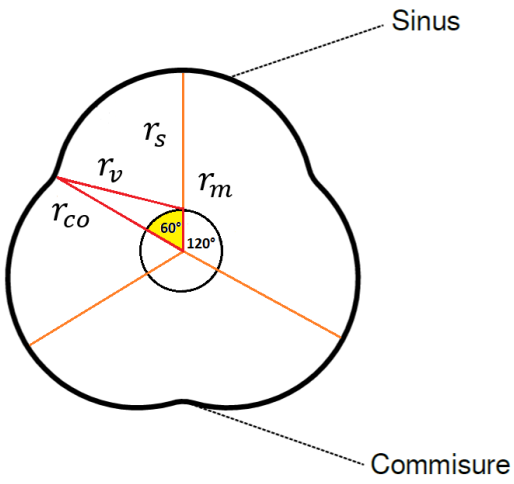

Figure A.1.1: Geometrical relationship between the constructive radii r_m, r_v and the sinus radius r_s and the commissure radius r_{co}. In the figure is underlined in yellow the angle of 60°comprised between the radius r_m and r_{co}.

Squaring (1) and (2) follows:

$$r_{co}^2 = \alpha_{co}^2 r_r^2$$

$$r_v^2 = \alpha_s^2 r_r^2 + r_m^2 - 2\alpha_s r_r r_m$$

and substituting (1) and (2) in (3):

$$\alpha_s^2 r_r^2 + r_m^2 - 2\alpha_s r_r r_m = \alpha_{co}^2 r_r^2 + r_m^2 - 2\alpha_{co} r_r r_m \cos 60°$$

that with reorganized terms can be written as follows:

$$r_m = \frac{r_r(\alpha_{co}^2 - \alpha_s^2)}{2\alpha_{co}\cos 60° - 2\alpha_s}$$

and making explicit cos 60°:

$$r_m = \frac{r_r(\alpha_{co}^2 - \alpha_s^2)}{\alpha_{co} - 2\alpha_s} \qquad (4)$$

Substituting (4) in equation (2) r_v con be rewritten as follows:

$$r_v = \alpha_s r_r - \frac{r_r(\alpha_{co}^2 - \alpha_s^2)}{\alpha_{co} - 2\alpha_s}$$

that gives:

$$r_v = \frac{r_r(\alpha_{co}\alpha_s - \alpha_{co}^2 - \alpha_s^2)}{\alpha_{co} - 2\alpha_s} \qquad (5)$$

A.2 Geometrical parameters in literature

In the following Table A.2.1 the scaling parameters considered by Swanson and Clark and Reul et al. are reported:

INPUT	Swanson Clark	Reul et al.
αs	1,38	1,55
αA	1	1,24
αL	0,71	1
αh1	0,17	0,34
αco	1	X

Table A.2.1: Scaling parameters considered in the work of Swanson and Clark and in the work of Reul et al.

In the following graphs (Fig. A.2.1, Fig. A.2.2, Fig. A.2.3, Fig. A.2.4) are reported in black the probability distribution showed in the article of Reul et al., in green the

values chosen for the experimental campaign and in blue the values suggested by Swanson and Clark. Furthermore, with brown is underlined the interval of values reported in the review of R. Haj-Ali et al.

In the graph A is reported the values of α_s, in graph B the values of α_A, in graph C the values of α_L, in graph D the values of α_{H1}. It must be noted that in graph D it is not reported the values of R. Haj-Ali et al. because the latter doesn't take into account this geometrical parameter in his work.

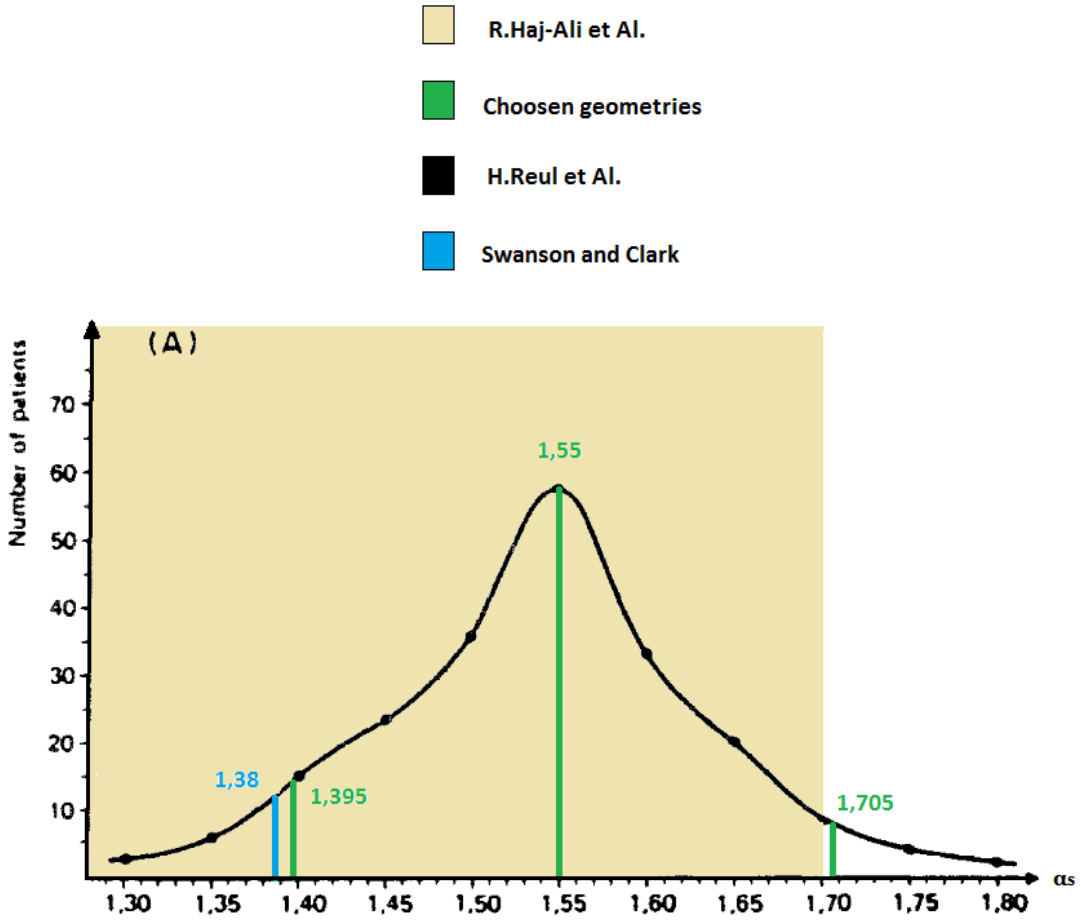

Figure A.2.1: Comparison between the value of the α_s geometrical parameter chosen in this work and the values reported in the cited literature.

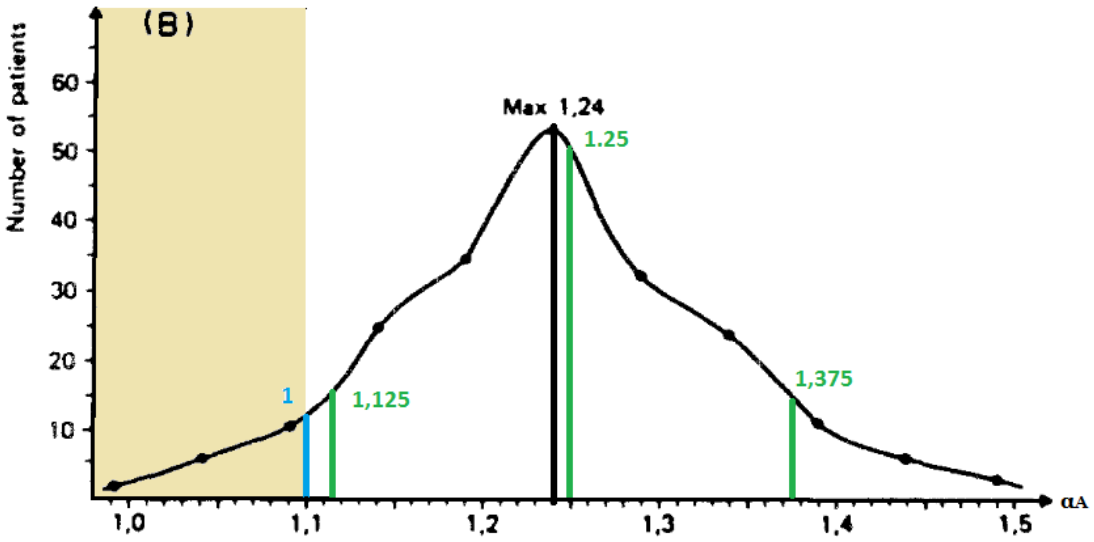

Figure A.2.2: Comparison between the value of the αA geometrical parameter chosen in this work and the values reported in the cited literature.

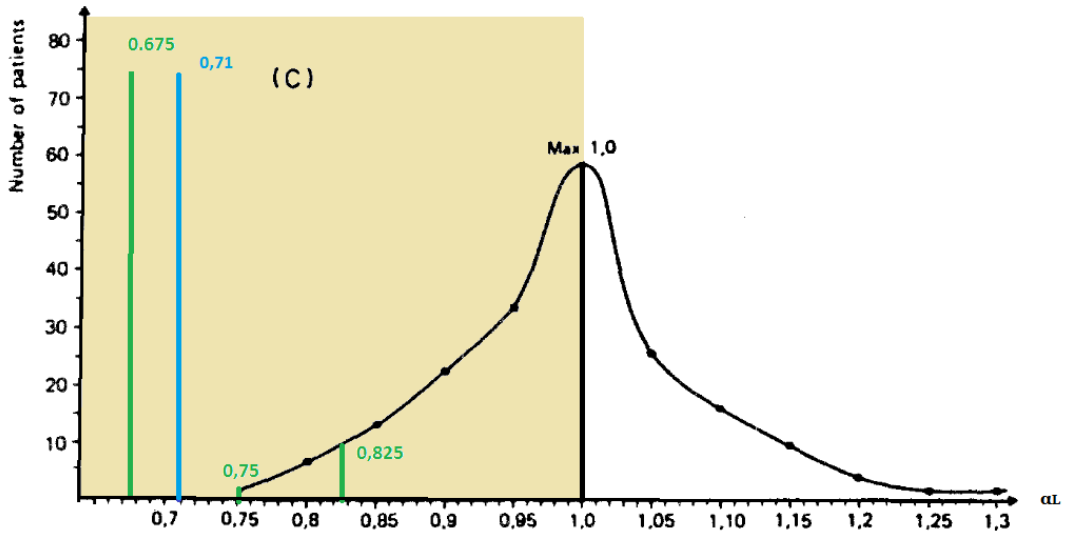

Figure A.2.3: Comparison between the value of the αL geometrical parameter chosen in this work and the values reported in the cited literature.

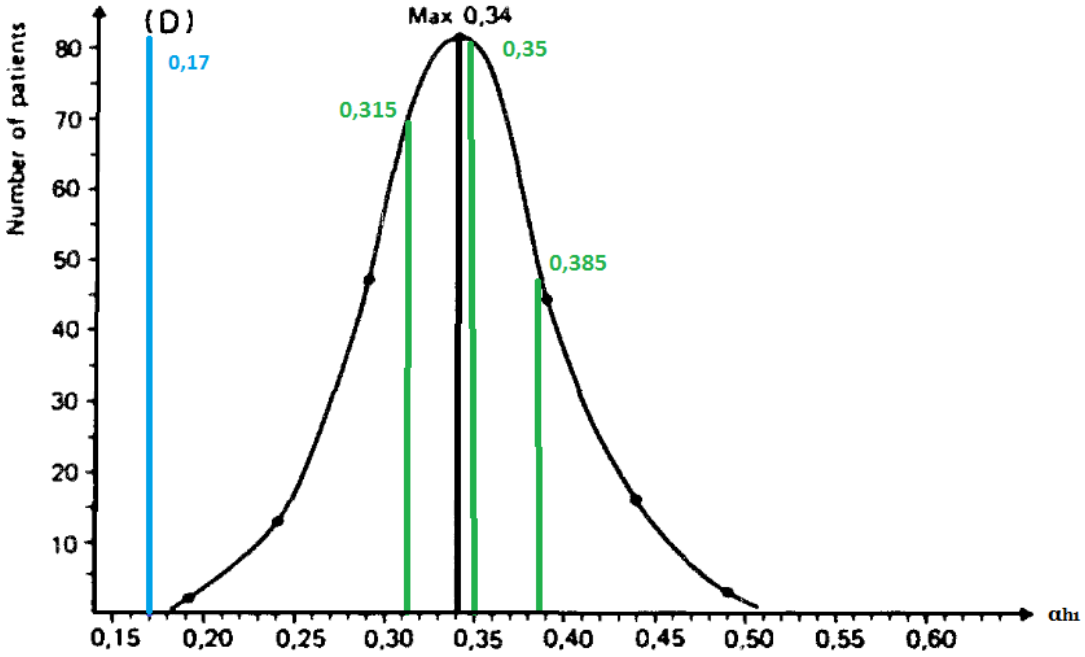

Figure A.2.4: Comparison between the value of the αh1 geometrical parameter chosen in this work and the values reported in the cited literature.

A.3 Silicon phantoms fabrication

For the fabrication of the three geometries of the silicon phantoms the following steps were followed:

3D printing

• Draw the simplified geometry of the inside wall of the phantom on Cad;
• Save as stl-file and 3D printing;

Surface treatment of model

• Sandpaper the surface;
• Spot filler the surface;
• Repeat (optional);
• Spray primer on the surface;
• Spray varnish on the surface;
• Clean and sterilize the surface;

Prepare casting mold

• Insert model in a casting plexiglass mold;

• Fix a funnel with hot clue to the casting plexiglass mold;

• Fix nozzle with hot clue to the casting plexiglass mold for the evacuation of air;

Prepare silicone

• Mix 1/10 in volume elastoil with 9/10 in volume of PDMS;

• Fill the prepared liquid silicone in a clean glass;

• Evacuate air bubbles from the liquid silicone with a vacuum pump;

• Pour the liquid silicone in a casting plexiglass mold until the mold is full;

Curing

• cure 24h with ambient air temperature or in the oven for 1h at 80°C;

Isolate silicone phantom

• Carefully remove the casting plexiglass mold using water and soap.

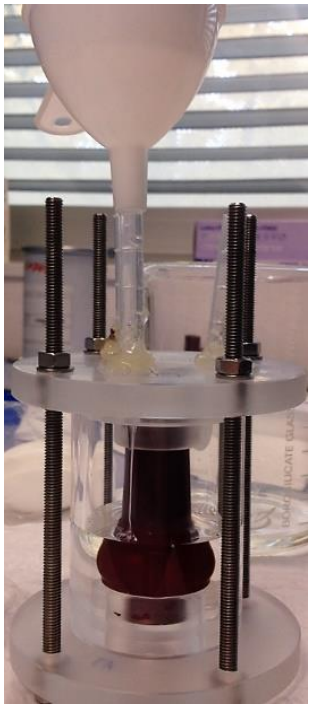

Figure A.3.1: Pouring of the liquid silicone in the casting plexiglass mold.

A.4 Refraction Index Matching (RIM)

To obtain the desiderated refraction index matching of the test fluid the fraction of water, glycerol and sodium chloride suggested in the work of D. S. Schmid [26] that minimize the distortion error was used.
In the Schmid's work the lowest distortion is associated with a fraction of 0,498 of water, 0,338 of glycerol and of 0,164 of sodium chloride.
These three components were mixed with a magnetic mixer until the salt and the glycerol were completely dissolved in the water.
To estimate the distortion error, reference pictures of a checkerboard immersed in the index matched fluid and pictures of the same immersed checkerboard with in front a silicon sample were acquired. The focus and the diaphragm aperture of the camera were tuned on the reference images and maintained constant to take the pictures with the silicon sample. The pictures were then processed in MATLAB with the Calibration Toolbox.
The distortion error was calculated as the displacement, in pixels, of the edges of the squares of the checkerboard in the image containing the sample with respect to the reference one.

Figure A.4.1: Quality RIM evaluation. Once the box containing the silicon sample is filled with RIM fluid the sample disappears. The sample is surrounded by air in the picture on the left, is half immersed in the picture in the middle and is completely immersed in the picture to the right.

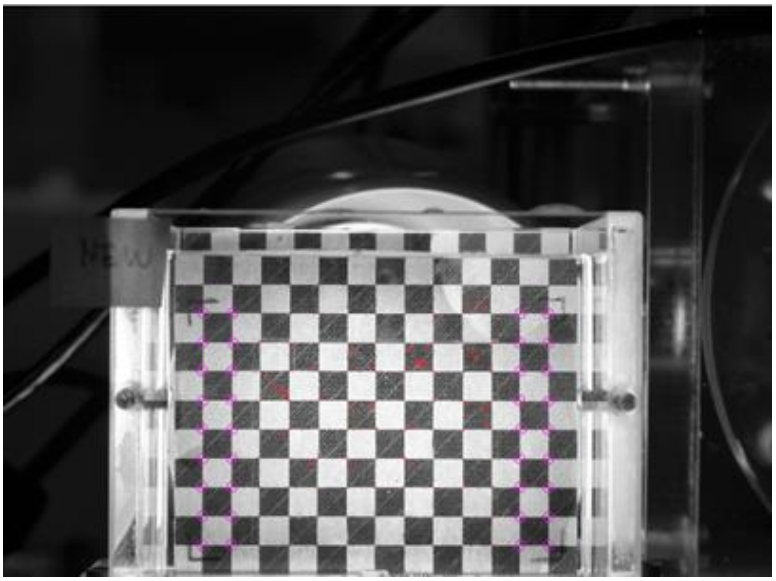

Figure A.4.2: Quality RIM evaluation. Output image of the MATLAB Calibration Toolbox underlining with red arrows the punctual distortion of the checkerboard present into the image due to the presence of the silicon sample.

A.5 Particles rest velocity estimation

Two forces act upon a spherical particle falling into a fluid: a downward force of gravity F_g and an upward drag force F_d.

The drag force F_d is given by the Stokes' Law:

$F_d = 6 * \pi * \mu_f * r_p * (u_f - u_p)$

where μ_f is the viscosity of the fluid, u_f is the velocity of the fluid, r_p is the radius of the particle and u_p is the terminal velocity of the particle when it is no longer accelerated.

The force of gravity F_g includes the weight force F_w and the buoyancy force F_b:

$F_g = F_w - F_b$

were F_w and $F_b$can be explicate as follows:

$F_w = \frac{4}{3} * \pi * r_p^3 * \rho_b * g$

$F_b = \frac{4}{3} * \pi * r_p^3 * \rho_f * g$

so that:

$F_g = \frac{4}{3} * \pi * r_p^3 * (\rho_b - \rho_f) * g$.

At terminal velocity $F_d = F_g$ because $F_d + F_g = m * a$ with $a = 0$, thus:

$$\frac{4}{3} * \pi * r_p^3 * (\rho_b - \rho_f) * g = 6 * \pi * \mu_f * r_p * (u_f - u_p)$$

and if the velocity of the fluid u_f is equal to zero the above equation can be solved with respect to the velocity u_p:

$$u_p = \frac{2}{9} * \frac{r_p^2}{\mu_f} * (\rho_p - \rho_f) * g$$

Using the values of the experimental campaign :

$r_p = 196 * 10^{-6}\, m$

$\mu_f = 5 * 10^{-3}\, Pa * s$

$\rho_p = 1220\ \frac{kg}{m^3}$

$\rho_f = 1210\ \frac{kg}{m^3}$

$g = 9.81 \frac{m}{s^2}$

the velocity of the particle at rest resulted to be

$$u_p = \frac{2}{9} * \frac{(196 * 10^{-6})^2}{5 * 10^{-3}} * (1220 - 1210) * 9.81 = 0{,}166 \frac{mm}{s}.$$

A.6 Camera calibration

The calibration consisted in referencing the three-dimensional coordinates of the test volume to the two-dimensional coordinates of the PHOTRON-ultima video camera view. Firstly, a checkerboard was placed in the measurement volume. Then, the whole test cell was filled with the RIM fluid to achieve the same experimental condition with the silicone phantom in place. Finally, a picture of the checkerboard was taken with the PHOTRON-ultima video camera.

For the experimental condition a full calibration of the camera was not necessary so that intrinsic and extrinsic parameters of the camera were not determined.

Indeed, the distance and the orientation of the camera with respect to the section test was known a priori and the distortion introduced by the silicon phantom was assumed to be higher than the distortion introduced by the lens of the camera itself.
For these reasons a simple scaling from pixels to meters was performed with MATLAB processing the calibration image with the script image_scales.m reported in Appendix A.10.

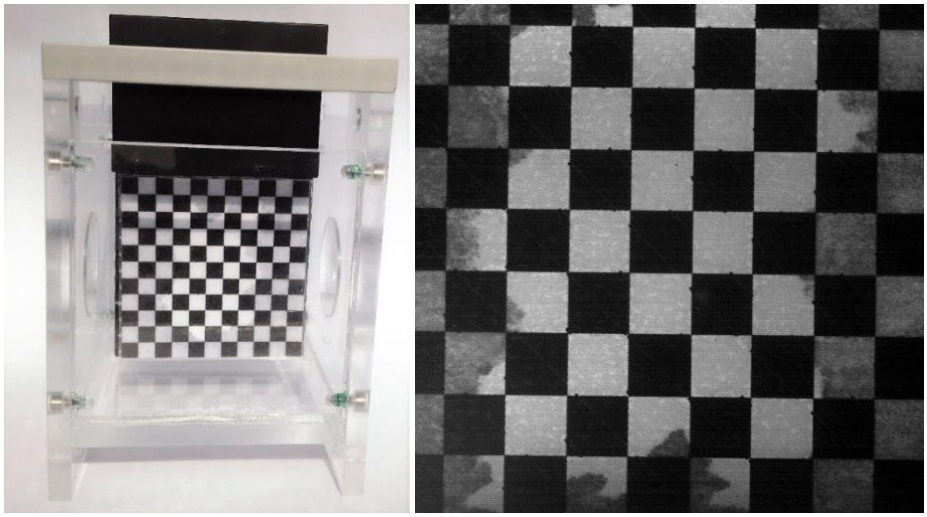

Figure A.6.1: Calibration checkerboard inserted in the plexiglass section test on the left and example of calibration image on the right.

A.7 Regions of interest (ROI)

The ROI were defined considering as invariant referments the tip of the leaflet at the maximum aperture, the silicon phantom and the sinotubular junction.
The sinus ROI was drown starting from the leaflet tip, following the leaflet at the maximum aperture and the shape of the sinus pocket until the sinotubular junction was reached. The starting point and the ending point of the line were then jointed to close the ROI.
The backflow ROI was drown starting from the leaflet tip, continuing horizontally for 300 pixels, creating a perpendicular angle to arrive to the silicon phantom and following it until the sinotubular junction was reached. The starting point and the ending point of the line were then jointed to close the ROI. It has to be noted that in a condition of perfect refractive index matching the phantom shouldn't be visible in the

images. Pictures showing the selected ROI for the sinus region and for the backflow region for each geometry are reported below (Fig. A.7.1, Fig. A.7.2 and Fig. A.7.3).

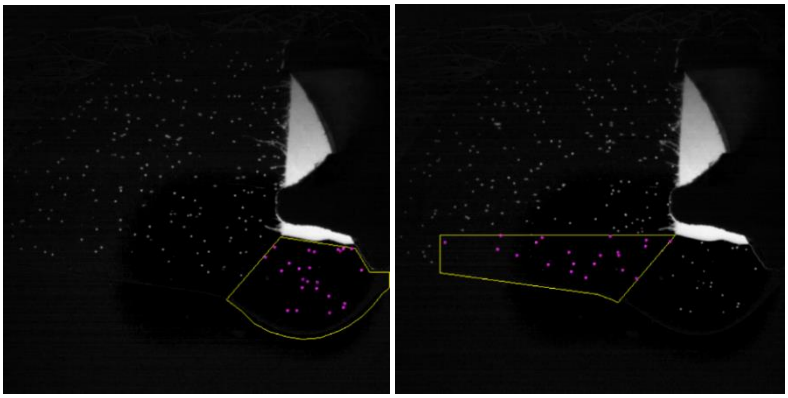

Figure A.7.1: Sinus and backflow ROI for the large geometry.

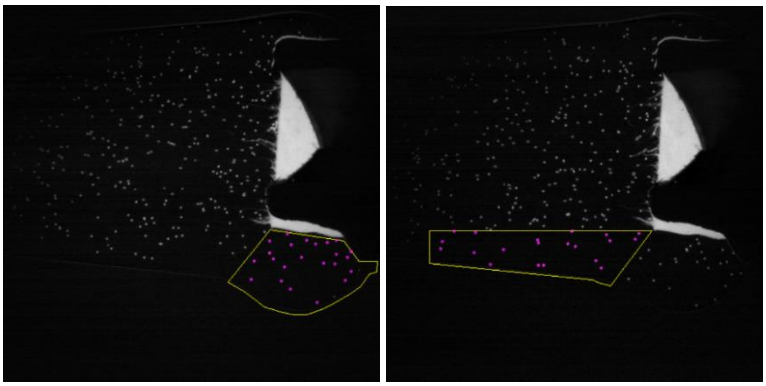

Figure A.7.2: Sinus and backflow ROI for the medium geometry.

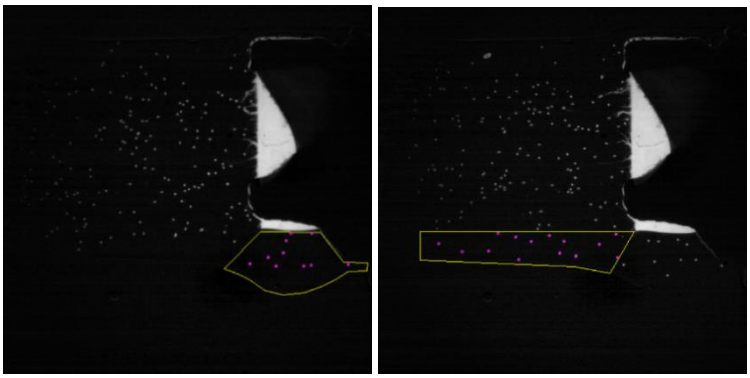

Figure A.7.3: Sinus and backflow ROI for the small geometry.

A.8 Jaquaman Linear Assignment Problem

According to the Jaquaman LAP framework particles linking happens in two steps: a frame to frame track segments creation and a track segments connection to achieve gap closing. The mathematical formulation used for both steps is linear assignment problem (LAP): a cost matrix containing all possible assignment costs is assembled. Actual assignments are retrieved by solving this matrix for minimal total cost.
In the first step, two consecutive frames are inspected for linking. Each spot of the first frame is offered to link to any other spot in the next frame, or not to link. This takes the shape of a (n+m) x (n+m) matrix (n is the number of spots in the frame t, m is the number of spots in the frame t+1), that can be divided in four quadrants.

- The top-left quadrant (size n x m) contains the costs for linking a spot i in the frame t to any spot j in the frame 't+1.
- The top-right quadrant (size n x n) contains the costs for a spot i in the frame t not to create a link with next frame (yielding a segment stop).
- The bottom-left quadrant (size m x m) contains the costs for a spot j in the frame t+1 not to have any link with previous frame (yielding a segment start).
- The bottom-right quadrant (size m x n) is the auxiliary block mathematically required by the LAP formalism. A detailed explanation for its existence is given in the supplementary note 3 of the paper of Jaquaman et al. [28]

To solve this LAP, Jaquaman and colleagues rely on the Munkres & Kuhn algorithm [29]. The algorithm returns the assignment list that minimizes the sum of their costs. The frame-to-frame linking described above is repeated first for all frame pairs. This yields a series of non-branching track segments. A track segment may be start or stop because of a missing detection, or because of a merge or split event, which is not taken into account at this stage but performed in the second step where track segments are offered to link between each other.
In the second step Jaquaman and colleagues proposes to exploit again the LAP framework for this step. A new cost matrix that resembles the first cost matrix, calculated for frame-to-frame linking, is generated. This time the following events are considered:

- The end of a track segment is offered to link to any other track segment start. This corresponds to gap-closing events, where a link is created typically over two spots separated by a missed detection.
- The start of a track segment is offered to link to the spots in the central part (not start, not end) of any other track segment. This corresponds to splitting events, where a track branches in two sub-tracks.
- The end of a track segment is offered to link to the spots in the central part of any other track segment. This corresponds to merging events, where two tracks merges into one.
- A spot part of any track segment is offered not to create any link.

The two steps Jaquaman LAP framework is schematized in the sketch of Fig. A.8.1.

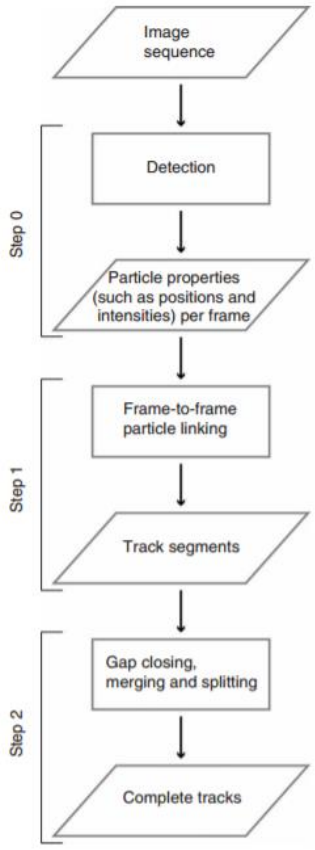

Figure A.8.1: Jaquaman LAP framework. Tracks are constructed from an image sequence by detecting particles in each frame (step 0), linking particles between consecutive frames (step 1) and then closing gaps and capturing merging and splitting events between the initial track segments (step 2).

A.9 Fiji Linear Assignment Problem

The implementation of the Fiji LAP is here reported in pseudo-language. It has to be noted that the word “link” means:

- Take all the source detections in frame t and the target detections in frame t+1.
- Compute the costs for all possible physical assignment (potential links) between source and target detections and store them in the cost matrix.
- Solve the LAP associated to this matrix.
- Create a link for each assignment found.

The particle linking algorithm would read as follow:

Initialization:

- Link all the detections of frame 0 to the detections of frame 1, just based on the square distance costs.
- From each of the m links newly created, compute a velocity. This velocity is used to initialize m Kalman filters.
- Initialize m tracks with the found detections and links, and store the associated Kalman filters.

Track elongation:

- For each Kalman filter, run the prediction step. This will generate m predicted positions.
- Link the m predicted positions to the n detections in frame 2, based on square distance.
- Target detection that have been linked to a predicted position are added to the corresponding track.
- The accepted target detection is used to run the update step of the Kalman filter.
- Loop to next frame.

Track termination:

- Some of the m predicted position might not find an actual detection to link to. In that case, we have an occlusion. The algorithm must decide whether it has to terminate the track or to bridge over a gap.

- If the number of successive occlusions for a Kalman filter is below a certain limit (typically 2 to 10), the track is not terminated, and the filter goes back to the track elongation step. Hopefully, from the new prediction a target particle will be found, and the detection in frame t will be linked to a detection in frame t+2 (or t+3 etc).
- Otherwise, the track is terminated and the Kalman filter object is dropped.

Track initiation:

- Conversely, some detections in frame t+1 might not be linked to a predicted position. In this case, these orphan detections are stored to initiate a new track. But for this, other orphans detections are needed in frame t+2.
- This step is identical to the initiation step, but for subsequent frames. It requires to store orphan detections in current and previous frames.
- In frame t+2, priority must be given to detections linked to the predicted positions by the Kalman filters over orphan detections of frame t+1. So when you deal with frame t+2, you perform first the track elongation step, get a list of orphan detections in frame t+2, and then combine it to the orphan detections in frame t+1 to initiate new Kalman filters.

As can be seen form the above reported pseudo-language the Fiji LAP is based on Jaquaman LAP described in the Appendix A.9 except for how the cost matrices are implemented and how the second step is performed.
In the Jaquaman LAP costs depend solely on the spot-to-spot distance but in the Fiji LAP is possible for the user to tune costs by adding penalties on spot features.
The user is asked for a maximal allowed linking distance (entered in physical units), and for a series of spot features, alongside with penalty weights. These parameters are used to tune the cost matrices. By adding feature penalties, the tracking problem results to be more robust.
In the second step, Jaqaman and colleagues proposes to exploit the same LAP to link the track segments between each other.
In the Fiji LAP each track initiated from a pair of spots in the first step is used to create an instance of a Kalman filter and generate a prediction of the most probable position of the particle. Then, all the predicted positions are linked against the actual spot positions in the frame using the square distance as costs.

A.10 Experimental Protocol

For every geometry 5 experiments in the same experimental conditions were conducted following the protocol reported below:

Set-up preparation

- preparation of the RIM fluid;
- connection of the PHOTRON-ultima video camera to the power supply, to the trigger output of the piston pump and to the computer throughout an Ethernet cable;
- connection of the Jai TM-6740 GE CCD camera to the power supply, to the signal generator and to the computer throughout an Ethernet cable;
- connection of the signal generator to the power supply and to the trigger output of the piston pump;
- mount the empty section test box in the same position that it will have during the experiment between the synthetic ventricle and the compliance chamber;
- start the computer and launch the PHOTRON-ultima video camera software;
- set the PHOTRON-ultima video camera at the established working condition:
  -distance of the objective from the section test: 30 cm;
  -aperture of the diaphragm: fully closed;
  -acquisition frame rate: 2000 frame/sec;
  -exposure time: 1/8000 sec;
  -sensitivity: db*4;
- fill with RIM fluid the section test box and position the checkerboard inside;
- position and turn on the LED light source to have enough light to illuminate the checkerboard;
- perform the calibration of the PHOTRON-ultima video camera using the checkerboard;
- remove the checkerboard, empty the section test box and remove it from the rest of the flow loop;
- connect the pressure pipes to the pressure sensors and turn on the Amplification Box;

- crimp the Edwards Intuity valve and fix it to the aluminum socket applying 4,5 atm into a balloon catheter positioned inside the stainless-steel frame of the valve;
- put the aluminum sealing rings on the silicon phantoms and position it inside the section test box;
- fix the silicon phantom inside the section test box putting at its extremity the two aluminum sockets. The socket holding the valve must be at the inlet of the silicon phantoms were there are the three sinuses of Valsava;
- orient the valve to have the commissures in the physiological position;
- screw the sealing rings around the silicon phantoms to fix the configuration and tightening it;
- screw the section test box with the silicon phantoms mounted in it to the compliance chamber and to the synthetic ventricle. The valve must be at the outlet of the synthetic ventricle;
- fill the piston pump with deionized water and close the pipe downstream the piston pump with a flexible membrane to separate the deionized water inside the pump from the test fluid circulating into the mock loop.
- connect the pump to the flow loop and launch Motion basic to control the piston pump;
- fill with index matched fluid the flow loop;
- remove the air activating the piston pump and using a catheter if necessary;
- launch the Jai Control Camera Tool;
- set the Jai TM-6740 GE CCD camera at the established working condition:
  - distance of the objective from the section test: slide the camera support on an aluminum rail until it engages the compliance chamber;
  -aperture of the diaphragm: fully closed;
  -acquisition frame rate: determined by the triggering signal coming from the signal generator;
  -exposure time: Async Programmable 200 μsec;
- set the signal generator at the established working condition: burns of 1000 rectangular pulses at 200 Hz with an amplitude of 5 volts from 0 to 5;
- calibrate the pressure sensors;

- connect the flowmeter on the pipe connecting the synthetic atrium to the synthetic ventricle just above the mitral mechanical valve;
- treatment of 0,6 g of microspheres with few droplets of TWEEN 20 in a test tube containing 12 ml of index matched fluid;
- set the piston pump at the established working condition:
  -frequency: 72 bpm;
  -maximum of the mean velocity over space at the systolic peak: 1 m/sec;
  -number of pulses: 50;
  -trigger signal: after the 30th pulse;

Acquisition

- start LabVIEW and start the acquisition of flow, pressure, trigger voltage and pump piston position;
- put the two cameras in acquisition mode such that they are waiting for the trigger signal to come;
- record;
- after 1,024 seconds stop the recording;

Data storing

- move the data stored in the PHOTRON-ultima video camera to the computer;
- save the acquired images with the two cameras both as Tiff images and Avi video;
- save the LabVIEW session and the excel calibration datasheet;

Images preprocessing

- compute the background with the MATLAB script compute_background.m;
- perform the background removal with the MATLAB script pre_process.m;

Particle tracking

- launch ImageJ (Fiji) and load the preprocessed images;
- define the region of interest (ROI),
- set tracking parameters as a function of the contrast between the particles and the background in the ROI;
- track the particles over all the preprocessed frames with the plugins Linear motion LAP tracker of ImageJ (Fiji);
- export as an .xml file the tracks computed with ImageJ (Fiji);

Tracks analysis

- import in MATLAB the .xml file and store it as an .m file with the MATLAB script save_tracks.m;
- compute the scaling from pxl/frame to m/sec trough the MATLAB script image_scales.m;
- analyze the tracks trough the MATLAB script analyze_tracks.m;
- plot velocity histogram of the velocities with the MATLAB script plot_track.m;

Results analysis

- To compare the three different geometries further postprocessing steps in MATLAB were conducted to obtain the mean velocity component U, V and the mean velocity magnitude M over the five experiments.
- To this end the MATLAB scripts mean_std_M.m, mean_std_U.m, mean_std_V.m, and plot_mean_velocities.m were used;
- Finally, to compute the mean resident time of particles and the mean number of tracks considered for each geometry the MATLAB script resident_time_percetages.m was used.

A.11 MATLAB scripts

compute_background.m

```
% This scripts computes the 'back-ground' in a sequence of images

clear all, close all, clc


% PARAMETERS
%--------------------------------------------------------------------------------

% data directories
raw_data_dir_name  =
'C:\Users\leona\Documents\Aortic_sinus_flow_analysis\DATA\LARGE_phantom\72bpm_120cmps
\05\cam001_C001S0001';

% image list
img_list = dir([raw_data_dir_name, '/*.tif']);
N_img = length(img_list);


% COMPUTE BACK-GROUND
%--------------------------------------------------------------------------------

for k = 1:500%N_img


    % read frame
    img = imread([raw_data_dir_name, '/', img_list(k).name]);
```

```
    % invert image
    img = imcomplement(img);

    [r, c] = size(img);

    if k==1
        img_bkgr = img;
    else
        for i = 1:c
            for j = 1:r

                if (img(j,i) < img_bkgr(j,i))
                    img_bkgr(j,i) = img(j,i);
                end
            end
        end
    end


end


% PLOT
%-------------------------------------------------------------------------------------
figure(1)

imshow(img_bkgr)


% SAVE
%-------------------------------------------------------------------------------------
imwrite(img_bkgr, [raw_data_dir_name, '\background.tif'])
```

pre_process.m

```
% This scripts reads raw images of a particle seeded flow and applies a few
% pre-processing steps on them.


clear all, close all, clc


% PARAMETERS
%-------------------------------------------------------------------------------------

% data directories
raw_data_dir_name    =
'C:\Users\leona\Documents\Aortic_sinus_flow_analysis\DATA\LARGE_phantom\72bpm_120cmps
\05\cam001_C001S0001'
prepro_data_dir_name =
'C:\Users\leona\Documents\Aortic_sinus_flow_analysis\DATA\LARGE_phantom\72bpm_120cmps
\05\prepro_cam001_C001S0001';

% image list
img_list = dir([raw_data_dir_name, '/cam001*.tif']);
N_img = length(img_list);

% bachround (has to be computed before)
img_bkgr = imread([raw_data_dir_name, '/background.tif']);

% PRE-PROCESS
%-------------------------------------------------------------------------------------

for k = 1:N_img


    % read frame
    img = imread([raw_data_dir_name, '/', img_list(k).name]);
```

```
    % invert image
    img = imcomplement(img);

    [r, c] = size(img);

    % remove background
    img = img -img_bkgr;

    % save
    imwrite(img, [prepro_data_dir_name, '/', img_list(k).name])

end

% PLOT
%-------------------------------------------------------------------------------
figure(1)

imshow(img)
```

save_tracks.m

```
% This scripts reads particle tracks (computed with the FIJI plug in track
% mate) from .xml file and stores as .mat file

clear all, close all, clc

% import tracks
[tracks, md] =
importTrackMateTracks('C:\Users\leona\Documents\Aortic_sinus_flow_analysis\DATA\LARGE
_phantom\tracks_sinus\5_Tracks.xml');

% save
save('particle_tracks','tracks', 'md')
```

image_scales.m

```
% pxl/frame -->  mm/msec

clear all, close all, clc

img = imread
('C:\Users\leona\Documents\Aortic_sinus_flow_analysis\DATA\MEDIUM_phantom\calibration
_middle\cam001_C001S0001\cam001_c001s0001000001.tif');

imshow(img);

[xp, yp] = ginput(2);
dpxl = sqrt((xp(2)-xp(1))^2 + (yp(2)-yp(1))^2)

promt = 'Enter length on checkerboard in milimiter: ';

dmm = input(promt)

scale_space = dmm/dpxl %mm/pxl

scale_time = (1/2000)*1000; %msec/frame

equivalenza_mm_msec = scale_space/scale_time;
equivalenza_m_sec = (scale_space/1000)/(scale_time/1000);
```

analyze_tracks.m

```
% With this script, particle track that are calculated with TrackMate (Fiji
% plugin) are further analyzed, by extracting certain statistics


clear all, close all, clc
```

```
% PARAMETERS
%-------------------------------------------------------------------------------------
t_start = 0
t_end   = 1667;
l = t_end-t_start;
dom_frame = [t_start+1:t_end];

% for convolution filter
hw = 3;
conv_mask = 1/(2*hw+1)*ones(1, 2*hw+1);


% LOAD PARTICLE TRACKS
%-------------------------------------------------------------------------------------
load('particle_tracks')


% deleta tracks from particle that entered and left sinus domain and which
% are shorter than threshold duration
dur_thrsh = 10;
del_counter = 0;
okey_ind = [];
duration_tracks= [];
for k = 1:length(tracks)

    % length of tracks in frames
    duration_tracks(k)=length(tracks{k}(:,1));

    % index of particles that enter and leave the sinus domain
    if (tracks{k}(1,1) > t_start) && (tracks{k}(end,1) < t_end)
        if tracks{k}(end,1) - tracks{k}(1,1) < dur_thrsh
            del_counter = del_counter + 1;
            continue
        end
    end

    okey_ind = [okey_ind, k];

end

tracks = tracks(okey_ind);

% number of tracks
N_tr = length(tracks);
dom_N_tr = [1:N_tr];

disp(['Total number of tracks: ', num2str(N_tr)])



% OVER-ALL STATS
%-------------------------------------------------------------------------------------

k_in_stay = [];
k_entered_stay = [];
k_in_left = [];
k_entered_left = [];
duration_tracks_in_left = [];
for k = 1:N_tr

    % index of particles that are initially inside the sinus domain and
    % stay inside
    if (tracks{k}(1,1) == t_start) && (tracks{k}(end,1) == t_end)
        k_in_stay = [k_in_stay, k];
    end


    % index of particles that enter the sinus domain and
    % stay inside
    if (tracks{k}(1,1) > t_start) && (tracks{k}(end,1) == t_end)
```

```
        k_entered_stay = [k_entered_stay, k];

    end

    % index of particles that are initially inside the sinus domain and
    % then leave
    if (tracks{k}(1,1) == t_start) && (tracks{k}(end,1) < t_end)
        duration_k= tracks{k}(end,1)- tracks{k}(1,1);
        duration_tracks_in_left=[duration_tracks_in_left, duration_k];
        k_in_left = [k_in_left, k];


    end

    % index of particles that enter and leave the sinus domain
    if (tracks{k}(1,1) > t_start) && (tracks{k}(end,1) < t_end)
        k_entered_left = [k_entered_left+1, k];
    end

end

disp(['# of inside, staying particles: ', num2str(length(k_in_stay)), ', (',
num2str(100*length(k_in_stay)/N_tr), ')'])
disp(['# of inside, leaving particles: ', num2str(length(k_in_left)), ', (',
num2str(100*length(k_in_left)/N_tr), ')'])
disp(['# of entering, staying particles: ', num2str(length(k_entered_stay)), ', (',
num2str(100*length(k_entered_stay)/N_tr), ')'])
disp(['# of entering, leaving particles: ', num2str(length(k_entered_left)), ', (',
num2str(100*length(k_entered_left)/N_tr), ')'])

% mean resident time in the sinus:
  total_time=sum(duration_tracks_in_left);
  mean_resident_time_frames=total_time/length(k_in_left);
  mean_resident_time_seconds=mean_resident_time_frames*0.0005;
  mean_std_resident_time=std(duration_tracks_in_left);

% VELOCITY STATS
%-------------------------------------------------------------------------------------

U = nan(N_tr, l);
V = nan(N_tr, l);
M = nan(N_tr, l);
STATS = zeros(N_tr,3);

%introduce calibration: from pxl/frame to m/sec :
promt = 'Enter calibration: ';
  calibration = input(promt);

for k = 1:N_tr

    t     = tracks{k}(:,1);
    x_pos = tracks{k}(:,2);
    y_pos = tracks{k}(:,3);

    % track end time (duration of the track)
    STATS(k,1) = t(end);

    % filter tracks
    x_pos = conv(x_pos, conv_mask, 'same');
    y_pos = conv(y_pos, conv_mask, 'same');

    % crop
    t_c   = t(hw+1:end-hw-1);
    x_pos = x_pos(hw+1:end-hw-1);
    y_pos = y_pos(hw+1:end-hw-1);

    % track length [pxl]
    STATS(k,2) = sum(sqrt(gradient(x_pos).^2 + gradient(y_pos).^2));

    % velocities [pxl/frame]
```

```
    u = gradient(x_pos);
    v = gradient(y_pos);
    m = sqrt(u.^2 + v.^2);

    % velocities [m/s]
    u = u*calibration;
    v = v*calibration;
    m = m*calibration;

    % mean velocity [m/s]
    STATS(k,3) = mean(m);


    % store
    t_ind_vec = t_c-t_start-hw+1;
    U(k,t_ind_vec) = u;
    V(k,t_ind_vec) = v;
    M(k,t_ind_vec) = m;

end
```

plot_tracks.m

```
% HISTOGRAM
nbins = 35;

% edge border for histogram (adjust with fac)
fac = 1.05;
eb = fac*max(M(:));

HU = zeros(l, nbins);
HV = zeros(l, nbins);
HM = zeros(l, nbins);

EU = zeros(l, nbins);
EV = zeros(l, nbins);
EM = zeros(l, nbins);

edgesU = linspace(-eb,eb,nbins+1);
edgesV = linspace(-eb,eb,nbins+1);
edgesM = linspace(0,eb,nbins+1);

for j = 1:l

    [hcU, eU] = histcounts(U(:,j), edgesU);
    [hcV, eV] = histcounts(V(:,j), edgesV);
    [hcM, eM] = histcounts(M(:,j), edgesM);

    HU(j,:) = hcU;
    HV(j,:) = hcV;
    HM(j,:) = hcM;

    EU(j,:) = (eU(1:end-1)+eU(2:end))/2;
    EV(j,:) = (eV(1:end-1)+eV(2:end))/2;
    EM(j,:) = (eM(1:end-1)+eM(2:end))/2;

end

[LX, LY] = meshgrid([1:nbins], dom_frame);

mean_U= mean (U,1,'omitnan');
mean_V= mean (V,1,'omitnan');
mean_M= mean (M,1,'omitnan');

% PLOTS
%--------------------------------------------------------------------------------
figure(1)

colormap jet
maxN = max(max([HU,HV,HM]));
minN = 0;
```

```
subplot 131
contourf(EU, LY, HU, 'linestyle', 'none');
caxis([minN,maxN]);
xlabel('U  [m/sec]');
ylabel('frames');
hold on
plot(mean_U, LY(:,1),'k','linewidth',0.75);
axis([-0.3,+0.3, t_start, t_end]);

subplot 132
contourf(EV, LY, HV, 'linestyle', 'none');
caxis([minN,maxN]);
xlabel('V  [m/sec]');
ylabel('frames');
hold on
plot(mean_V, LY(:,1),'k','linewidth',0.75);
axis([-0.3,+0.3, t_start, t_end]);



subplot 133
contourf(EM, LY, HM, 'linestyle', 'none');
caxis([minN,maxN]);
xlabel('M  [m/sec]');
ylabel('frames');
hold on
plot(mean_M, LY(:,1),'k','linewidth',0.75);
axis([EM(1,1),+0.3, t_start, t_end]);
colorbar;
```

mean_std_U.m

```
% mean velocity and standard deviation of U velocity [m/sec]
mean_U1= mean (U1,1,'omitnan');
std_U1= std(U1,1,1,'omitnan');

mean_U2= mean (U2,1,'omitnan');
std_U2= std(U2,1,1,'omitnan');

mean_U3= mean (U3,1,'omitnan');
std_U3= std(U3,1,1,'omitnan');

mean_U4= mean (U4,1,'omitnan');
std_U4= std(U4,1,1,'omitnan');

mean_U5= mean (U5,1,'omitnan');
std_U5= std(U5,1,1,'omitnan');

% mean of the mean velocities and mean of the standard deviations [m/sec]

U=[mean_U1;mean_U2;mean_U3;mean_U4;mean_U5];
mean_U=mean(U,1,'omitnan');

STD=[std_U1;std_U2;std_U3;std_U4;std_U5]
std_U= mean(STD,1,'omitnan');

%-------------------------------------------------------------------------------------
%calculate mean U velocity and standard deviation for a first frame interval:

start_frame= 650;
end_frame= 950;
selected_frames_interval=end_frame-start_frame;


for j=start_frame:end_frame
mean_interval(j)= mean_U(j);
std_interval(j)= std_U(j);
end

for K=1:start_frame
```

```
mean_interval(K)= nan;
std_interval(K)= nan;
end

MEAN_INTERVAL_U_650_950= mean(mean_interval,'omitnan');
MEAN_STD_INTERVAL_U_650_950=mean(std_interval,'omitnan');

%-------------------------------------------------------------------------------------
%calculate mean U velocity and standard deviation for a second frame interval:

start_frame= 1200;
end_frame= 1400;
selected_frames_interval=end_frame-start_frame;


for j=start_frame:end_frame
mean_interval(j)= mean_U(j);
std_interval(j)= std_U(j);
end

for K=1:start_frame
mean_interval(K)= nan;
std_interval(K)= nan;
end

MEAN_INTERVAL_U_1200_1400= mean(mean_interval,'omitnan');
MEAN_STD_INTERVAL_U_1200_1400=mean(std_interval,'omitnan');
```

mean_std_V.m

```
% mean velocity and standard deviation of V velocity [m/sec]
mean_V1= mean (V1,1,'omitnan');
std_V1= std(V1,1,1,'omitnan');

mean_V2= mean (V2,1,'omitnan');
std_V2= std(V2,1,1,'omitnan');

mean_V3= mean (V3,1,'omitnan');
std_V3= std(V3,1,1,'omitnan');

mean_V4= mean (V4,1,'omitnan');
std_V4= std(V4,1,1,'omitnan');

mean_V5= mean (V5,1,'omitnan');
std_V5= std(V5,1,1,'omitnan');

% mean of the mean velocities and mean of the standard deviations [m/sec]

V=[mean_V1;mean_V2;mean_V3;mean_V4;mean_V5];
mean_V=mean(V,1,'omitnan');

STD=[std_V1;std_V2;std_V3;std_V4;std_V5]
std_V= mean(STD,1,'omitnan');

%-------------------------------------------------------------------------------------
%calculate mean V velocity and standard deviation for a first frame interval:

start_frame= 650;
end_frame= 950;
selected_frames_interval=end_frame-start_frame;


for j=start_frame:end_frame
mean_interval(j)= mean_V(j);
std_interval(j)= std_V(j);
end

for K=1:start_frame
mean_interval(K)= nan;
```

```
std_interval(K)= nan;
end

MEAN_INTERVAL_V_650_950= mean(mean_interval,'omitnan');
MEAN_STD_INTERVAL_V_650_950=mean(std_interval,'omitnan');
%-------------------------------------------------------------------------------------------
%calculate mean V velocity and standard deviation for a second frame interval:

start_frame= 1200;
end_frame= 1400;
selected_frames_interval=end_frame-start_frame;

for j=start_frame:end_frame
mean_interval(j)= mean_V(j);
std_interval(j)= std_V(j);
end

for K=1:start_frame
mean_interval(K)= nan;
std_interval(K)= nan;
end

MEAN_INTERVAL_V_1200_1400= mean(mean_interval,'omitnan');
MEAN_STD_INTERVAL_V_1200_1400=mean(std_interval,'omitnan');
```

mean_std_M.m

```
% mean velocity and standard deviation of M velocity [m/sec]
mean_M1= mean (M1,1,'omitnan');
std_M1= std(M1,1,1,'omitnan');

mean_M2= mean (M2,1,'omitnan');
std_M2= std(M2,1,1,'omitnan');

mean_M3= mean (M3,1,'omitnan');
std_M3= std(M3,1,1,'omitnan');

mean_M4= mean (M4,1,'omitnan');
std_M4= std(M4,1,1,'omitnan');

mean_M5= mean (M5,1,'omitnan');
std_M5= std(M5,1,1,'omitnan');

% mean of the mean velocities and mean of the standard deviations [m/sec]

M=[mean_M1;mean_M2;mean_M3;mean_M4;mean_M5];
mean_M=mean(M,1,'omitnan');

STD=[std_M1;std_M2;std_M3;std_M4;std_M5]
std_M= mean(STD,1,'omitnan');

%-------------------------------------------------------------------------------------------
%calculate mean M velocity and standard deviation for a first frame interval:

start_frame= 650;
end_frame= 950;
selected_frames_interval=end_frame-start_frame;

for j=start_frame:end_frame
mean_interval(j)= mean_M(j);
std_interval(j)= std_M(j);
end

for K=1:start_frame
mean_interval(K)= nan;
std_interval(K)= nan;
end

MEAN_INTERVAL_M_650_950= mean(mean_interval,'omitnan');
```

```
MEAN_STD_INTERVAL_M_650_950=mean(std_interval,'omitnan');
%-------------------------------------------------------------------------------
%calculate mean M velocity and standard deviation for a second frame interval:

start_frame= 1200;
end_frame= 1400;
selected_frames_interval=end_frame-start_frame;

for j=start_frame:end_frame
mean_interval(j)= mean_M(j);
std_interval(j)= std_M(j);
end

for K=1:start_frame
mean_interval(K)= nan;
std_interval(K)= nan;
end

MEAN_INTERVAL_M_1200_1400= mean(mean_interval,'omitnan');
MEAN_STD_INTERVAL_M_1200_1400=mean(std_interval,'omitnan');
```

plot_mean_velocities.m

```
close all;
clc;

figure (1)
plot(mean_M_LARGE);
hold on
plot(mean_M_MIDDLE);
hold on
plot(mean_M_SMALL);
legend('LARGE [m/s]','MIDDLE [m/s]','SMALL [m/s]')
xlabel('frames');
hold on
title('mean M velocity');


figure (2)
plot(mean_U_LARGE);
hold on
plot(mean_U_MIDDLE);
hold on
plot(mean_U_SMALL);
legend('LARGE [m/s]','MIDDLE [m/s]','SMALL [m/s]')
xlabel('frames');
hold on
title('mean U velocity');


figure (3)
plot(mean_V_LARGE);
hold on
plot(mean_V_MIDDLE);
hold on
plot(mean_V_SMALL);
legend('LARGE [m/s]','MIDDLE [m/s]','SMALL [m/s]')
xlabel('frames');
hold on
title('mean V velocity');
```

resident_time_percentages.m

```
% mean of the mean resident time [sec]:LARGE geometry

large_mean_resident_time_vector=[large_1,large_2,large_3,large_4,large_5];
LARGE_MEAN_RESIDENT_TIME= mean(large_mean_resident_time_vector)*0.0005;

% mean of the std of resident time [sec]:LARGE geometry
```

```
large_mean_std_resident_time_vector=[large_std_1,large_std_2,large_std_3,large_std_4,
large_std_5];
LARGE_MEAN_STD_RESIDENT_TIME= mean(large_mean_std_resident_time_vector)*0.0005;

%-------------------------------------------------------------------------------------
% mean of the mean resident time [sec]:MEDIUM geometry

medium_mean_resident_time_vector=[medium_1,medium_2,medium_3,medium_4,medium_5];
MEDIUM_MEAN_RESIDENT_TIME= mean(medium_mean_resident_time_vector)*0.0005;

% mean of the std of resident time [sec]:LARGE geometry

medium_mean_std_resident_time_vector=[medium_std_1,medium_std_2,medium_std_3,medium_s
td_4,medium_std_5];
MEDIUM_MEAN_STD_RESIDENT_TIME= mean(medium_mean_std_resident_time_vector)*0.0005;

%-------------------------------------------------------------------------------------
% mean of the mean resident time [sec]:SMALL geometry

small_mean_resident_time_vector=[small_1,small_2,small_3,small_4,small_5];
SMALL_MEAN_RESIDENT_TIME= mean(small_mean_resident_time_vector)*0.0005;

% mean of the std of resident time [sec]:LARGE geometry

small_mean_std_resident_time_vector=[large_std_1,large_std_2,large_std_3,large_std_4,
large_std_5];
SMALL_MEAN_STD_RESIDENT_TIME= mean(small_mean_std_resident_time_vector)*0.0005;

%-------------------------------------------------------------------------------------
% mean number of paticle tracked
K=(k1+k2+k3+k4+k5)/5;

% mean number of particles IN-IN [%]
 L1=100*length(k_in_stay1)/k1;
 L2=100*length(k_in_stay2)/k2;
 L3=100*length(k_in_stay3)/k3;
 L4=100*length(k_in_stay4)/k4;
 L5=100*length(k_in_stay5)/k5;

 L_IN_iN=(L1+L2+L3+L4+L5)/5;

 % mean number of particles OUT-IN [%]
 L1=100*length(k_entered_stay1)/k1;
 L2=100*length(k_entered_stay2)/k2;
 L3=100*length(k_entered_stay3)/k3;
 L4=100*length(k_entered_stay4)/k4;
 L5=100*length(k_entered_stay5)/k5;

 L_OUT_IN=(L1+L2+L3+L4+L5)/5;

  % mean number of particles IN-OUT [%]
 L1=100*length(k_in_left1)/k1;
 L2=100*length(k_in_left2)/k2;
 L3=100*length(k_in_left3)/k3;
 L4=100*length(k_in_left4)/k4;
 L5=100*length(k_in_left5)/k5;

 L_IN_OUT=(L1+L2+L3+L4+L5)/5;

  % mean number of particles OUT-OUT [%]
 L1=100*length(k_entered_left1)/k1;
 L2=100*length(k_entered_left2)/k2;
 L3=100*length(k_entered_left3)/k3;
 L4=100*length(k_entered_left4)/k4;
 L5=100*length(k_entered_left5)/k5;

 L_OUT_OUT=(L1+L2+L3+L4+L5)/5;
```

fluttering.m

```
%this script compute the fluttering frequency of the leaflet from a direct
observation of the timing of the sinus V velocity peaks :

A=[34,38,43,23,70,44,93,50];
M= mean (A);
time= M/2000;
frequency= 1/time;
```

particles_tracks.m

```
% This scripts reads raw images of a particle seeded flow and produces a
% single image with the track of a particle for a certain time
% span.

clear all, close all, clc


% PARAMETERS
%--------------------------------------------------------------------------------------

% data directory
data_dir_name =
'C:\Users\leona\Documents\Aortic_sinus_flow_analysis\DATA\SMALL_phantom\72bpm_100cmps
\04\prepro_cam001_C001S0001';

% image list
img_list = dir([data_dir_name, '/*.tif']);

% time span start and end (frames)
ts       = 20;
ts_start = 780;
ts_end   = ts_start + ts;

% threshold
thrsh = 30;

% color map for tacks
cmap = colormap('cool');
cmap_inkr = size(cmap, 1)/ts;

% READ AND PROCESS
%--------------------------------------------------------------------------------------

% initial frame
img = imread([data_dir_name, '/', img_list(ts_start).name]);

img_rgb = cat(3, img, img, img);
for k = ts_start+1:ts_end

    % read frame
    img = imread([data_dir_name, '/', img_list(k).name]);

    % process frame
    img(img < thrsh) = 0;

    % mask
    mask = img >= thrsh;

    % assign color
    img_r = img;
    img_r(mask) = img(mask)*cmap(ceil(cmap_inkr*(k-ts_start)), 1);

    img_g = img;
    img_g(mask) = img(mask)*cmap(ceil(cmap_inkr*(k-ts_start)), 2);

    img_b = img;
    img_b(mask) = img(mask)*cmap(ceil(cmap_inkr*(k-ts_start)), 3);

    % make color image
    img_rgb = img_rgb + cat(3, img_r, img_g, img_b);
```

```
end


% PLOT
%-------------------------------------------------------------------------------
figure(1)

imshow(img_rgb)


% SAVE
%-------------------------------------------------------------------------------
print('tracks', '-dpng')
```